# Multiple-relaxation-time lattice Boltzmann kinetic model for combustion

Aiguo Xu,[1,2,3,*] Chuandong Lin,[4] Guangcai Zhang,[1,3,5] and Yingjun Li[4,†]

[1]*National Key Laboratory of Computational Physics, Institute of Applied Physics and Computational Mathematics, P. O. Box 8009-26, Beijing 100088, People's Republic of China*

[2]*Center for Applied Physics and Technology, MOE Key Center for High Energy Density Physics Simulations, College of Engineering, Peking University, Beijing 100871, People's Republic of China*

[3]*State Key Laboratory of Explosion Science and Technology, Beijing Institute of Technology, Beijing 100081, People's Republic of China*

[4]*State Key Laboratory for GeoMechanics and Deep Underground Engineering, China University of Mining and Technology, Beijing 100083, People's Republic of China*

[5]*State Key Laboratory of Theoretical Physics, Institute of Theoretical Physics, Chinese Academy of Sciences, Beijing 100190, People's Republic of China*

(Received 23 November 2014; published 27 April 2015)

To probe both the hydrodynamic nonequilibrium (HNE) and thermodynamic nonequilibrium (TNE) in the combustion process, a two-dimensional multiple-relaxation-time (MRT) version of lattice Boltzmann kinetic model (LBKM) for combustion phenomena is presented. The chemical energy released in the progress of combustion is dynamically coupled into the system by adding a chemical term to the LB kinetic equation. Aside from describing the evolutions of the conserved quantities, the density, momentum, and energy, which are what the Navier-Stokes model describes, the MRT-LBKM presents also a coarse-grained description on the evolutions of some nonconserved quantities. The current model works for both subsonic and supersonic flows with or without chemical reaction. In this model, both the specific-heat ratio and the Prandtl number are flexible, the TNE effects are naturally presented in each simulation step. The model is verified and validated via well-known benchmark tests. As an initial application, various nonequilibrium behaviors, including the complex interplays between various HNEs, between various TNEs, and between the HNE and TNE, around the detonation wave in the unsteady and steady one-dimensional detonation processes are preliminarily probed. It is found that the system viscosity (or heat conductivity) decreases the local TNE, but increases the global TNE around the detonation wave, that even locally, the system viscosity (or heat conductivity) results in two kinds of competing trends, to increase and to decrease the TNE effects. The physical reason is that the viscosity (or heat conductivity) takes part in both the thermodynamic and hydrodynamic responses.

DOI: 10.1103/PhysRevE.91.043306 PACS number(s): 47.11.−j, 47.40.Rs, 47.70.−n

## I. INTRODUCTION

Combustion has long been playing a dominant role in the transportation and power generation. More than 80% of world energy is from various combustion processes. For the foreseeable future it will remain to be the major energy conversion process [1]. At the same time, the low energy conversion efficiency of existing combustion engines has been becoming the major source of air pollution and driving force for climate change [2]. Roughly speaking, there are two kinds of fuels, the nuclear fuel and the organic fuel. The latter contains the organic materials such as hydrocarbon natural fuel and artificial fuel after processing. Various medical wastes [3] belong to the organic fuel. To achieve low emissions, fuel lean and high speed combustion, and enable new engine technologies, in recent years, some new combustion concepts, such as pulsed and spinning detonation engines [4,5], microscale combustion [6,7] and nanopropellants [8,9], partially premixed and stratified combustion [10], plasma assisted combustion [11–13], and cool flames [14], have been proposed and developed.

However, there are still a number of problems, for example, (i) for spinning detonation, the influences of the wall curvature and fuel-air mixing on the detonation initiation and propagation modes, (ii) for high pressure stratified combustion, the ignition to detonation transition at low temperature, (iii) for plasma assisted combustion, the highly nonequilibrium energy transfer between electrons, electronically and vibrationally excited molecules, and neutral molecules, (iv) for cool flames, the hydrodynamics, chemical kinetics, and kinetics-transport coupling, are challenging our current understanding [1,15–17]. All these new combustion concepts involve complicated nonequilibrium chemical and transport processes.

For a long time, the main way people know the combustion process is experimental and theoretical research [18–24]. In recent five decades, the numerical simulation of combustion process has achieved great success [24–28]. To simulate a combustion process, the following steps are needed: (i) establish a physical model; (ii) establish discrete control equations; (iii) numerical experiments and data analysis. Generally speaking, for a combustion system, there are three levels of description which are in the microscopic, mesoscopic, and macroscopic scales, respectively. The microscopic scale is generally referred to the description at molecular dynamic (MD) level. The main numerical tool is the MD simulation. Via study at this level, the reaction rate equation can be established. The macroscopic scale is generally referred to the description based on Navier-Stokes equations. At this level, the mainly concerned are hydrodynamic nonequilibrium (HNE) behaviors, specifically, the evolutions of the density, temperature, flow

*Corresponding author: Xu_Aiguo@iapcm.ac.cn
†Corresponding author: lyj@aphy.iphy.ac.cn

 

velocity, and pressure. The mesoscopic description is generally referred to the description based on the gas kinetic theory, more specifically, the Boltzmann equation. At this level, we can study more details of the interfacial structures and the interplay between the HNE and the thermodynamic nonequilibrium (TNE) behaviors.

What is used in the most engineering applications is the macroscopic or hydrodynamic description. The physical model at this level consists of some specific form of the hydrodynamic equations coupled with some phenomenological reaction rate equation, which is constructed according to the conservation laws of mass, momentum, and energy, as well as some suitable simplifications. To establish the discrete control equations, the first step is to choose a coordinate system where the coordinate axes should adapt to the edge of the computational and physical domains. When the computational domain is rectangular, cylindrical, or conical, the generally chosen coordinate system can be orthogonal, cylindrical, or spherical. The second step is to establish a structured, unstructured, or block-structured grid according to the specific situation. The third step is to choose or formulate a discretization scheme. The frequently used schemes include the finite difference (FD), the finite volume, the finite element, the finite analytic [29], the boundary element, the integration transformation, the spectral method, etc.

In the recent three decades, the lattice Boltzmann (LB) method [30–49] has been becoming a powerful tool to simulate various complex flows. Due to the importance of combustion phenomena, one can find a number of LB papers in literature [50–67]. The pioneering LB model for combustion systems was given by Succi *et al.* [50] in 1997. This work is based on the assumptions of fast chemistry and cold flames with weak heat release. In the following years, Filippova and Hänel [51–53] proposed a kind of hybrid scheme for low Mach number reactive flows. The flow field is solved by modified lattice Bhatnagar-Gross-Krook (BGK) method and the transport equations for energy and species are solved by a FD scheme. Via the LB method, Yu *et al.* [54] simulated scalar mixing in a multicomponent flow and a chemical reacting flow. Yamamoto *et al.* [55] constructed a LB scheme for combustion phenomena including the reaction, diffusion, and convection effects. Lee *et al.* [58] presented a double-distribution function LB model to solve the laminar diffusion flames within the context of Burke-Schumann flame sheet model. In recent years, Chen *et al.* [60,61] developed a coupled LB method for the low Mach number combustion and presented some meaningful results [62–67].

In brief, LB modeling of combustion phenomena has long been an interesting topic, but was mainly focused on low Mach number combustion where the incompressible LB model works. In those studies, the LB model works as a kind of alternative scheme to recover the hydrodynamic model. In those thermal LB models, the temperature $T$ could not be described by the same distribution function (DF) which describes the density $\rho$ and flow velocity $\mathbf{u}$. In some LB models, it was further assumed that the chemical reaction has no effect on the flow field.

As a special case of combustion, the explosion phenomena lead to accidents or disasters sometimes. But the controlled explosion has been widely applied in various engineering problems, such as explosion painting, explosion cleaning, explosion working, explosion propulsion, demolition blasting, blasting mining, blasting excavation, etc. The traditional computational fluid dynamics (CFD) has been used to simulate explosion for many years. It is interesting to extend the LB model to simulate such complex phenomena. As a special discretization of the Boltzmann equation, the appropriately designed LB model should possess more kinetic information which is beyond the description of the Navier-Stokes equations. For convenience of description, we refer such a LB kinetic model as to LBKM.

To model a more practical combustion phenomenon, an appropriate LBKM should be thermal, compressible, and work for both the low and the high Mach number flows. At the same time, the chemical reaction and flow behavior should couple naturally. In such a LBKM, the density $\rho$, flow velocity $\mathbf{u}$, temperature $T$, and relevant higher-order kinetic moments should be described by the same DF. It should work as a physical tool to probe both the HNE and TNE [33,44,68].

In recent years, the development of LB models for high speed compressible flows [69–77] makes it possible to simulate systems with shock wave. Very recently we presented two LBKMs for high Mach combustion and detonation phenomena [78,79]. The first is in Cartesian coordinates [78]. The second [79] is in polar coordinate system and designed for simulating the explosion and implosion behaviors. Both the two models are based on the single-relaxation-time (SRT) BGK-Boltzmann equation. Consequently, the Prandtl number (Pr), is fixed at 1. To make the Prandtl number flexible, a solution is to use a multiple-relaxation-time (MRT) version of the LBKM. Early in 1989, Higuera, Succi, and Benzi developed a strategy for building suitable collision operators [30], which is the precursor of MRT models [31,32,74,75,80]. In this work, we present a MRT-LBKM for low and high Mach number combustion phenomena. In this model, the viscosity and heat conductivity can be adjusted independently. More importantly, the model can be used to track the TNE effects and investigate the interplay between the HNE and TNE behaviors.

The rest of the paper is organized as follows. In Sec. II, the MRT-LBKM for combustion phenomena is formulated. In Sec. III, the Chapman-Enskog analysis is performed. The validation and verification of the model are presented in Sec. IV. Some discussions on the physical gains and computing costs of various LB models are shown in Sec. V. In Sec. VI, the model is used to probe some fine structures of the detonation wave. Section VII summarizes and concludes this paper.

## II. FORMULATION OF THE LATTICE BOLTZMANN KINETIC MODEL

The practical combustion process is very complicated. To study some fundamental behaviors in the combustion system, in this work we propose a simple LBKM described by the following equation:

$$\frac{\partial f_i}{\partial t} + v_{i\alpha}\frac{\partial f_i}{\partial r_\alpha} = -M_{il}^{-1}\left[\hat{R}_{lk}\left(\hat{f}_k - \hat{f}_k^{eq}\right) + \hat{A}_l\right] + C_i, \quad (1)$$

$$C_i = \left.\frac{df_i}{dt}\right|_C, \quad (2)$$

where $i$ (= 1,2,...,$N$) is the index of discrete velocity, $N$ is the total number of the discrete velocities used in the LBKM, $f_i$ is the discrete distribution function, $v_{i\alpha}$ is the $\alpha$ component of the $i$th discrete velocity, $\alpha = x,\ y$; $\hat{f}_k = M_{ki} f_i$ ($\hat{f}_k^{eq} = M_{ki} f_i^{eq}$) is the moment of the (equilibrium) distribution function and formally the (equilibrium) distribution function in the moment space; $M_{ki}$ is the element of the matrix $\mathbf{M}$ connecting the vector of discrete distribution function $\mathbf{f} = (f_1, f_2, \ldots, f_N)^T$, and the vector $\hat{\mathbf{f}} = (\hat{f}_1, \hat{f}_2, \ldots, \hat{f}_N)^T$; $\hat{\mathbf{R}} = \mathbf{MRM}^{-1} = \mathrm{diag}(R_1, R_2, \ldots, R_N)$ is a diagonal matrix whose element $R_k$ describes speed of $\hat{f}_k$ approaching $\hat{f}_k^{eq}$; $\hat{A}_l$ is the $l$th element of $\hat{\mathbf{A}} = (0,\ldots,0,\hat{A}_8,\hat{A}_9,0,\ldots,0)^T$ and is a modification to the collision operator $\hat{R}_{lk}(\hat{f}_k - \hat{f}_k^{eq})$, where

$$\hat{A}_8 = \rho T \frac{R_5 - R_8}{R_5}\left[4u_x\left(\frac{\partial u_x}{\partial x} - \frac{1}{D+I}\frac{\partial u_x}{\partial x} - \frac{1}{D+I}\frac{\partial u_y}{\partial y}\right) + 2u_y\left(\frac{\partial u_y}{\partial x} + \frac{\partial u_x}{\partial y}\right)\right], \tag{3}$$

$$\hat{A}_9 = \rho T \frac{R_7 - R_9}{R_7}\left[4u_y\left(\frac{\partial u_y}{\partial y} - \frac{1}{D+I}\frac{\partial u_x}{\partial x} - \frac{1}{D+I}\frac{\partial u_y}{\partial y}\right) + 2u_x\left(\frac{\partial u_y}{\partial x} + \frac{\partial u_x}{\partial y}\right)\right]. \tag{4}$$

The reason for this modification is as follows. Although from the mathematical point of view, the relaxation coefficient $R_k$ can be independently adjusted for each kinetic mode ($\hat{f}_k - \hat{f}_k^{eq}$), from the physical point of view, coupling may exist between or among different kinetic modes. To ensure the MRT model can present correct macroscopic behavior, one can perform the Chapman-Enskog analysis and analyze the consistency of the terms describing transportation in the recovered hydrodynamic equations to find a solution for the modification to the collision term [75]. This modification is added so that the LBKM can recover the consistent Navier-Stokes equations in the hydrodynamic limit. $C_i$ is the chemical term added to the LB equation and will be given a specific form in the following part. For convenience of description below, we introduce $A_i = M_{il}^{-1}\hat{A}_l$. In this work, we consider a two-dimensional ($D = 2$) system where the particle mass is unity. The discrete equilibrium distribution function satisfies the following relations:

$$\sum f_i^{eq} = \rho = \sum f_i, \tag{5}$$

$$\sum f_i^{eq} v_{i\alpha} = \rho u_\alpha = \sum f_i v_{i\alpha}, \tag{6}$$

$$\sum f_i^{eq}\left(v_i^2 + \eta_i^2\right) = \rho[(D+I)T + u^2] = \sum f_i\left(v_i^2 + \eta_i^2\right), \tag{7}$$

$$\sum f_i^{eq} v_{i\alpha} v_{i\beta} = \rho(\delta_{\alpha\beta} T + u_\alpha u_\beta), \tag{8}$$

$$\sum f_i^{eq}\left(v_i^2 + \eta_i^2\right) v_{i\alpha} = \rho u_\alpha[(D+I+2)T + u^2], \tag{9}$$

$$\sum f_i^{eq} v_{i\alpha} v_{i\beta} v_{i\chi} = \rho(u_\alpha\delta_{\beta\chi} + u_\beta\delta_{\chi\alpha} + u_\chi\delta_{\alpha\beta})T + \rho u_\alpha u_\beta u_\chi, \tag{10}$$

$$\sum f_i^{eq}\left(v_i^2 + \eta_i^2\right) v_{i\alpha} v_{i\beta} = \rho\delta_{\alpha\beta}[(D+I+2)T + u^2]T + \rho u_\alpha u_\beta[(D+I+4)T + u^2], \tag{11}$$

$$\sum f_i^{eq}\eta_i^2 v_{i\alpha} v_{i\beta} = \rho\delta_{\alpha\beta} I T^2 + \rho u_\alpha u_\beta I T, \tag{12}$$

$$\sum f_i^{eq}\left(v_i^2 + \eta_i^2\right)\eta_i^2 = \rho I T[u^2 + (D+3I)T], \tag{13}$$

$$\sum f_i^{eq}\left(v_i^2 + \eta_i^2\right) v_i^2 v_{i\alpha} = \rho u_\alpha[u^4 + (D+2)(D+I+4)T^2 + (2D+I+8)u^2 T], \tag{14}$$

$$\sum f_i^{eq}\left(v_i^2 + \eta_i^2\right)\eta_i^2 v_{i\alpha} = \rho u_\alpha I T[u^2 + (D+3I+2)T], \tag{15}$$

where $\rho$, $T$, $p$ ($=\rho T$), and $u_\alpha$ are the density, temperature, pressure, and velocity, respectively. Aside from the translational degrees of freedom, $\eta_i$ is a free parameter introduced to describe the $I$ extra degrees of freedom corresponding to molecular rotation and/or internal vibration. The internal kinetic energy per unit volume is $E = \rho(D+I)T/2$.

Actually, Eqs.(5)–(15) can be uniformly written in a matrix form, i.e.,

$$\mathbf{M} \times \mathbf{f}^{eq} = \hat{\mathbf{f}}^{eq}, \tag{16}$$

where the boldface symbols $\mathbf{f}^{eq} = (f_1^{eq}, f_2^{eq}, \ldots, f_N^{eq})^T$ and $\hat{\mathbf{f}}^{eq} = (\hat{f}_1^{eq}, \hat{f}_2^{eq}, \ldots, \hat{f}_N^{eq})^T$ denote $N$-dimensional column vectors. The matrix $\mathbf{M} = (\mathbf{M}_1, \mathbf{M}_2, \ldots, \mathbf{M}_N)^T$, $\mathbf{M}_i = (m_{i1}, m_{i2}, \ldots, m_{iN})$, where $m_{1i} = 1$, $m_{2i} = v_{ix}$, $m_{3i} = v_{iy}$, $m_{4i} = v_i^2 + \eta_i^2$, $m_{5i} = v_{ix}^2$, $m_{6i} = v_{ix}v_{iy}$, $m_{7i} = v_{iy}^2$, $m_{8i} = (v_i^2 + \eta_i^2)v_{ix}$, $m_{9i} = (v_i^2 + \eta_i^2)v_{iy}$, $m_{10i} = v_{ix}^3$, $m_{11i} = v_{ix}^2 v_{iy}$, $m_{12i} = v_{ix}v_{iy}^2$, $m_{13i} = v_{iy}^3$, $m_{14i} = (v_i^2 + \eta_i^2)v_{ix}^2$, $m_{15i} = (v_i^2 + \eta_i^2)v_{ix}v_{iy}$, $m_{16i} = (v_i^2 + \eta_i^2)v_{iy}^2$, $m_{17i} = \eta_i^2 v_{ix}^2$, $m_{18i} = \eta_i^2 v_{ix}v_{iy}$, $m_{19i} = \eta_i^2 v_{iy}^2$, $m_{20i} = (v_i^2 + \eta_i^2)\eta_i^2$, $m_{21i} = (v_i^2 + \eta_i^2)v_i^2 v_{ix}$, $m_{22i} = (v_i^2 + \eta_i^2)v_i^2 v_{iy}$, $m_{23i} = (v_i^2 + \eta_i^2)\eta_i^2 v_{ix}$, $m_{24i} = (v_i^2 + \eta_i^2)\eta_i^2 v_{iy}$. Correspondingly, $\hat{f}_1^{eq} = \rho$, $\hat{f}_2^{eq} = \rho u_x$, $\hat{f}_3^{eq} = \rho u_y$, $\hat{f}_4^{eq} = \rho[(D+I)T + u^2]$, $\hat{f}_5^{eq} = \rho(T + u_x^2)$, $\hat{f}_6^{eq} = \rho u_x u_y$, $\hat{f}_7^{eq} = \rho(T + u_y^2)$, $\hat{f}_8^{eq} = \rho u_x[(D+I+2)T + u^2]$, $\hat{f}_9^{eq} = \rho u_y[(D+I+2)T + u^2]$, $\hat{f}_{10}^{eq} = 3\rho u_x T + \rho u_x^3$, $\hat{f}_{11}^{eq} = \rho u_y T + \rho u_x^2 u_y$, $\hat{f}_{12}^{eq} = \rho u_x T + \rho u_x u_y^2$, $\hat{f}_{13}^{eq} = 3\rho u_y T + \rho u_y^3$, $\hat{f}_{14}^{eq} = \rho[(D+I+2)T + u^2]T + \rho u_x^2[(D+I+4)T + u^2]$, $\hat{f}_{15}^{eq} = \rho u_x u_y[(D+I+4)T + u^2]$, $\hat{f}_{16}^{eq} = \rho[(D+I+2)T + u^2]T + \rho u_y^2[(D+I+4)T + u^2]$, $\hat{f}_{17}^{eq} = \rho I T^2 + \rho u_x^2 I T$, $\hat{f}_{18}^{eq} = \rho u_x u_y I T$, $\hat{f}_{19}^{eq} = \rho I T^2 + \rho u_y^2 I T$, $\hat{f}_{20}^{eq} = \rho I T[u^2 + (D+3I)T]$, $\hat{f}_{21}^{eq} = \rho u_x[u^4 + (D+2)(D+I+4)T^2 + (2D+I+8)u^2 T]$, $\hat{f}_{22}^{eq} = \rho u_y[u^4 + (D+2)(D+I+4)T^2 + (2D+I+8)u^2 T]$, $\hat{f}_{23}^{eq} = \rho u_x I T[u^2 + (D+3I+2)T]$, $\hat{f}_{24}^{eq} = \rho u_y I T[u^2 + (D+3I+2)T]$.

Formally, compared with the MRT version of the LBKM for high speed compressible flows [74,75], the second term $C_i$ in the right sides of Eq. (1) describes the variation of distribution function due to the chemical reaction.

The actual combustion processes are very complicated. In this work, we consider the simple combustion processes and present a simple LBKM based on the following assumptions:

(1) The flow behavior is described by a single distribution function $f$. The relaxation coefficient $R_k$ can be roughly regarded as a constant, where $k = 1, 2, \ldots, N$.

(2) The radiative heat loss is negligible.

(3) The reaction process is irreversible and described by an empirical or semiempirical equation

$$\lambda' = \frac{d\lambda}{dt} = F(\lambda), \tag{17}$$

where $\lambda = \rho_p/\rho$ is the concentration of the reaction product in the system and denotes the progress of the reaction; $\rho_p$ is the density of the reaction product; $\rho$ is the density of the whole system.

(4) The chemical energy is directly transformed into the internal energy in the following form:

$$\left.\frac{dE}{dt}\right|_C = \rho Q \lambda', \tag{18}$$

where $Q$ is the amount of heat released by the chemical reactant per unit mass.

(5) The chemical reaction is slow enough, compared with kinetic process of approaching thermodynamic equilibrium, so that

$$\left.\frac{df}{dt}\right|_C \approx \left.\frac{df^{eq}}{dt}\right|_C. \tag{19}$$

The chemical reaction results only in the increase of local temperature $T$ and the local density $\rho$ and hydrodynamic velocity $\mathbf{u}$ remain unchanged. Thus,

$$\left.\frac{df^{eq}}{dt}\right|_C = \left.\frac{\partial f^{eq}}{\partial T}\frac{dT}{dt}\right|_C. \tag{20}$$

The equilibrium distribution function $f^{eq}$ used here reads as

$$f^{eq} = \rho\left(\frac{1}{2\pi T}\right)^{D/2}\left(\frac{1}{2\pi IT}\right)^{1/2}\exp\left[-\frac{(\mathbf{v}-\mathbf{u})^2}{2T} - \frac{\eta^2}{2IT}\right], \tag{21}$$

which gives

$$\frac{\partial f^{eq}}{\partial T} = \frac{-(1+D)IT + I(\mathbf{v}-\mathbf{u})^2 + \eta^2}{2IT^2} f^{eq}. \tag{22}$$

It is easy to get

$$\left.\frac{dT}{dt}\right|_C = \frac{2Q}{D+I}F(\lambda) \tag{23}$$

from the relation $E = \rho(D+I)T/2$ and Eqs. (17) and (18). Substituting Eqs. (22) and (23) into (20) gives

$$C_i = f_i^{eq}\, Q \frac{-(1+D)IT + I(\mathbf{v}_i-\mathbf{u})^2 + \eta_i^2}{I(D+I)T^2} F(\lambda). \tag{24}$$

Equations (1) can be rewritten as 24 coupled equations in the two-dimensional case. Consequently, we need a discrete velocity model (DVM) with at least 24 discrete velocities. To obtain the high computational efficiency, we choose the following two-dimensional DVM which only has 24 discrete velocities (see Fig. 1):

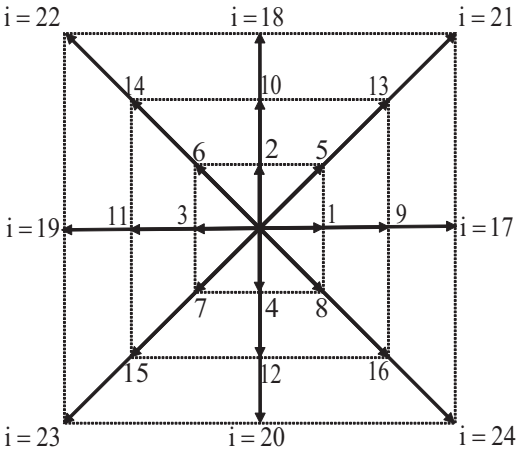


FIG. 1. Schematic of the discrete velocity model.

$$\bar{\mathbf{v}}_i = \begin{cases} \text{cyc}: & (\pm 1, 0) & \text{for} & 1 \leqslant i \leqslant 4, \\ \text{cyc}: & (\pm 1, \pm 1) & \text{for} & 5 \leqslant i \leqslant 8, \end{cases} \tag{25}$$

$$\mathbf{v}_i = \begin{cases} v_a \bar{\mathbf{v}}_i & \text{for} & 1 \leqslant i \leqslant 8, \\ v_b \bar{\mathbf{v}}_{i-8} & \text{for} & 9 \leqslant i \leqslant 16, \\ v_c \bar{\mathbf{v}}_{i-16} & \text{for} & 17 \leqslant i \leqslant 24, \end{cases} \tag{26}$$

$$\eta_i = \begin{cases} \eta_a & \text{for} & 1 \leqslant i \leqslant 8, \\ \eta_b & \text{for} & 9 \leqslant i \leqslant 16, \\ \eta_c & \text{for} & 17 \leqslant i \leqslant 24, \end{cases} \tag{27}$$

where cyc indicates the cyclic permutation. For convenience of description, we refer the two-dimensional DVM with 24 discrete velocities as to D2V24.

It has been known that the spurious oscillations occurring near shock wave with finite-difference equations are related to the dispersion term in the corresponding modified differential equations. If the sign of the dispersion coefficient, say $\nu$, is properly adjusted, that is, the sign changes across shock wave, $\nu > 0$ upstream and $\nu < 0$ downstream, the undesirable oscillations can be totally suppressed. Therefore, in this work, the spatial derivatives in Eq. (1) are calculated by adopting the nonoscillatory and nonfree-parameters dissipative (NND) finite-difference scheme [81]. The evolution of chemical process is described by

$$\frac{\partial \lambda}{\partial t} + u_\alpha \frac{\partial \lambda}{\partial r_\alpha} = \omega_1 p^m (1-\lambda) + \omega_2 p^n \lambda (1-\lambda), \tag{28}$$

where the so-called Cochran's rate function [82] is adopted for the description of chemical reaction; $\omega_1$, $\omega_2$, $m$, and $n$ are adjustable parameters. Without losing generality, the ignition temperature $T_{ig} = 1.1$ is assumed in this work. Only when $T > T_{ig}$ can the chemical reaction proceed. And we choose the parameters $m = n = 1$. The temporal derivative in Eq. (28) is solved analytically, and the spatial ones by the NND scheme [81].

The inverse of the matrix $\mathbf{M}$ can be analytically solved by the software MATLAB2011. It should be pointed out that, although the complete formulas seems long and complicated,

in practical simulations, the parameters $(v_a, v_b, v_c, \eta_a, \eta_b, \eta_c)$ are replaced by specific values, then the elements of matrix $\mathbf{M}$ and its inverse $\mathbf{M}^{-1}$ are fixed also by specific values before the main loop.

## III. CHAPMAN-ENSKOG ANALYSIS OF THE MODEL

The Chapman-Enskog analysis shows that, only if $\mathbf{f}^{eq}$ satisfies the statistical relation (16) or, specifically, the 11 equations (5)–(15), then the LB equation (1) can recover the Navier-Stokes model for combustion. We show the main procedure of the Chapman-Enskog analysis in the following.

From Eq. (1), we get

$$\frac{\partial \hat{\mathbf{f}}}{\partial t} + \frac{\partial}{\partial r_\alpha}(\hat{\mathbf{E}}_\alpha \hat{\mathbf{f}}) = -\hat{\mathbf{R}}(\hat{\mathbf{f}} - \hat{\mathbf{f}}^{eq}) + \hat{\mathbf{A}} + \hat{\mathbf{C}}, \tag{29}$$

where $\hat{\mathbf{C}} = \mathbf{MC}$, $\hat{\mathbf{E}}_\alpha = \mathbf{M}\mathbf{v}_\alpha\mathbf{M}^{-1}$, and $\mathbf{v}_\alpha = \mathrm{diag}(v_{1\alpha}, v_{2\alpha}, \ldots, v_{N\alpha})$ is a diagonal matrix.

Expanding the variables with respect to $\varepsilon$ corresponding the Knudsen number, as

$$\begin{aligned} f_i &= f_i^{(0)} + f_i^{(1)} + f_i^{(2)} + \ldots, \\ A_i &= A_{1i}, \\ C_i &= C_{1i}, \\ \frac{\partial}{\partial t} &= \frac{\partial}{\partial t_1} + \frac{\partial}{\partial t_2}, \\ \frac{\partial}{\partial r_\alpha} &= \frac{\partial}{\partial r_{1\alpha}}, \end{aligned} \tag{30}$$

where the part of distribution function $f_i^{(l)} = \mathrm{O}(\varepsilon^l)$, the modification term $A_{1i} = \mathrm{O}(\varepsilon)$, the chemical term $C_{1i} = \mathrm{O}(\varepsilon)$, the partial derivatives $\partial/\partial t_l = \mathrm{O}(\varepsilon^l)$ and $\partial/\partial r_{1\alpha} = \mathrm{O}(\varepsilon)$, $(l = 1,2,\ldots)$. It is easy to get from the first three subequations of Eq. (30) that

$$\hat{f}_i = \hat{f}_i^{(0)} + \hat{f}_i^{(1)} + \hat{f}_i^{(2)} + \ldots, \tag{31}$$

$$\hat{A}_i = \hat{A}_{1i}, \tag{32}$$

$$\hat{C}_i = \hat{C}_{1i}. \tag{33}$$

By substituting the last two subequations of (30) and Eqs. (31)–(33) into (29) and comparing the coefficients of the same order of $\varepsilon$, we have

$$\mathrm{O}(\varepsilon^0): \quad \hat{\mathbf{f}}^{(0)} = \hat{\mathbf{f}}^{eq}, \tag{34}$$

$$\mathrm{O}(\varepsilon^1): \quad \left(\frac{\partial}{\partial t_1} + \hat{\mathbf{E}}_\alpha \frac{\partial}{\partial r_{1\alpha}}\right)\hat{\mathbf{f}}^{(0)} = -\hat{\mathbf{R}}\hat{\mathbf{f}}^{(1)} + \hat{\mathbf{A}} + \hat{\mathbf{C}}, \tag{35}$$

$$\mathrm{O}(\varepsilon^2): \quad \frac{\partial}{\partial t_2}\hat{\mathbf{f}}^{(0)} + \left(\frac{\partial}{\partial t_1} + \hat{\mathbf{E}}_\alpha \frac{\partial}{\partial r_{1\alpha}}\right)\hat{\mathbf{f}}^{(1)} = -\hat{\mathbf{R}}\hat{\mathbf{f}}^{(2)}, \tag{36}$$

where $\mathbf{f}^{(l)} = (f_1^{(l)}, f_2^{(l)}, \ldots, f_N^{(l)})^T$. Specifically, $\mathbf{f}^{(0)}$ is the matrix for the equilibria of the moments, $\mathbf{f}^{(1)}$ and $\mathbf{f}^{(2)}$ are the matrices for the first order and second order deviations from equilibria.

From Eq. (35), we get

$$\frac{\partial \hat{f}_1^{eq}}{\partial t_1} + \frac{\partial \hat{f}_2^{eq}}{\partial x_1} + \frac{\partial \hat{f}_3^{eq}}{\partial y_1} = -R_1 \hat{f}_1^{(1)} + \hat{C}_1, \tag{37}$$

$$\frac{\partial \hat{f}_2^{eq}}{\partial t_1} + \frac{\partial \hat{f}_5^{eq}}{\partial x_1} + \frac{\partial \hat{f}_6^{eq}}{\partial y_1} = -R_2 \hat{f}_2^{(1)} + \hat{C}_2, \tag{38}$$

$$\frac{\partial \hat{f}_3^{eq}}{\partial t_1} + \frac{\partial \hat{f}_6^{eq}}{\partial x_1} + \frac{\partial \hat{f}_7^{eq}}{\partial y_1} = -R_3 \hat{f}_3^{(1)} + \hat{C}_3, \tag{39}$$

$$\frac{\partial \hat{f}_4^{eq}}{\partial t_1} + \frac{\partial \hat{f}_8^{eq}}{\partial x_1} + \frac{\partial \hat{f}_9^{eq}}{\partial y_1} = -R_3 \hat{f}_4^{(1)} + \hat{C}_4, \tag{40}$$

$$\frac{\partial \hat{f}_5^{eq}}{\partial t_1} + \frac{\partial \hat{f}_{10}^{eq}}{\partial x_1} + \frac{\partial \hat{f}_{11}^{eq}}{\partial y_1} = -R_5 \hat{f}_5^{(1)} + \hat{C}_5, \tag{41}$$

$$\frac{\partial \hat{f}_6^{eq}}{\partial t_1} + \frac{\partial \hat{f}_{11}^{eq}}{\partial x_1} + \frac{\partial \hat{f}_{12}^{eq}}{\partial y_1} = -R_6 \hat{f}_6^{(1)} + \hat{C}_6, \tag{42}$$

$$\frac{\partial \hat{f}_7^{eq}}{\partial t_1} + \frac{\partial \hat{f}_{12}^{eq}}{\partial x_1} + \frac{\partial \hat{f}_{13}^{eq}}{\partial y_1} = -R_7 \hat{f}_7^{(1)} + \hat{C}_7, \tag{43}$$

$$\frac{\partial \hat{f}_8^{eq}}{\partial t_1} + \frac{\partial \hat{f}_{14}^{eq}}{\partial x_1} + \frac{\partial \hat{f}_{15}^{eq}}{\partial y_1} = -R_8 \hat{f}_8^{(1)} + \hat{A}_8 + \hat{C}_8, \tag{44}$$

$$\frac{\partial \hat{f}_9^{eq}}{\partial t_1} + \frac{\partial \hat{f}_{15}^{eq}}{\partial x_1} + \frac{\partial \hat{f}_{16}^{eq}}{\partial y_1} = -R_9 \hat{f}_9^{(1)} + \hat{A}_9 + \hat{C}_9. \tag{45}$$

It is easy to get from Eqs. (5)–(15) and (24) that $\hat{C}_1 = 0$, $\hat{C}_2 = 0$, $\hat{C}_3 = 0$, $\hat{C}_4 = 2\rho\lambda' Q$, $\hat{C}_5 = 2\rho\lambda' Q/(D+I)$, $\hat{C}_6 = 0$, $\hat{C}_7 = 2\rho\lambda' Q/(D+I)$, $\hat{C}_8 = 2\rho u_x\lambda' Q(D+I+2)/(D+I)$, $\hat{C}_9 = 2\rho u_y\lambda' Q(D+I+2)/(D+I)$. Substituting all the specific forms of $\hat{C}_i$ and $\hat{f}_i^{eq}$ into (37)–(45) gives

$$\frac{\partial \rho}{\partial t_1} + \frac{\partial j_x}{\partial x_1} + \frac{\partial j_y}{\partial y_1} = 0, \tag{46}$$

$$\frac{\partial j_x}{\partial t_1} + \frac{\partial \rho\left(T + u_x^2\right)}{\partial x_1} + \frac{\partial \rho u_x u_y}{\partial y_1} = 0, \tag{47}$$

$$\frac{\partial j_y}{\partial t_1} + \frac{\partial \rho u_x u_y}{\partial x_1} + \frac{\partial \rho\left(T + u_y^2\right)}{\partial y_1} = 0, \tag{48}$$

$$\begin{aligned} &\frac{\partial \xi}{\partial t_1} + \frac{\partial \rho u_x[(D+I+2)T + u^2]}{\partial x_1} \\ &\quad + \frac{\partial \rho u_y[(D+I+2)T + u^2]}{\partial y_1} = 2\rho\lambda' Q, \end{aligned} \tag{49}$$

$$\begin{aligned} &\frac{\partial \rho\left(T + u_x^2\right)}{\partial t_1} + \frac{\partial \rho\left(3u_x T + u_x^3\right)}{\partial x_1} + \frac{\partial \rho\left(u_y T + u_x^2 u_y\right)}{\partial y_1} \\ &\quad = -R_5 \hat{f}_5^{(1)} + \rho\lambda' Q \frac{2}{D+I}, \end{aligned} \tag{50}$$

$$\begin{aligned} &\frac{\partial \rho u_x u_y}{\partial t_1} + \frac{\partial \rho\left(u_y T + u_x^2 u_y\right)}{\partial x_1} + \frac{\partial \rho\left(u_x T + u_x u_y^2\right)}{\partial y_1} \\ &\quad = -R_6 \hat{f}_6^{(1)}, \end{aligned} \tag{51}$$

$$\frac{\partial\rho\left(T+u_y^2\right)}{\partial t_1}+\frac{\partial\rho\left(u_xT+u_xu_y^2\right)}{\partial x_1}+\frac{\partial\rho\left(3u_y+u_y^3\right)}{\partial y_1}$$
$$=-R_7\hat{f}_7^{(1)}+\frac{2\rho\lambda'Q}{D+I}, \tag{52}$$

$$\frac{\partial\rho u_x[(D+I+2)T+u^2]}{\partial t_1}+\frac{\partial}{\partial x_1}\{\rho[(D+I+2)T+u^2]T+\rho u_x^2[(D+I+4)T+u^2]\}+\frac{\partial\rho u_xu_y[(D+I+4)T+u^2]}{\partial y_1}$$
$$=-R_8\hat{f}_8^{(1)}+\hat{A}_8+2\rho u_x\lambda'Q\frac{D+I+2}{D+I}, \tag{53}$$

$$\frac{\partial\rho u_y[(D+I+2)T+u^2]}{\partial t_1}+\frac{\partial}{\partial y_1}\{\rho[(D+I+2)T+u^2]T+\rho u_y^2[(D+I+4)T+u^2]\}+\frac{\partial\rho u_xu_y[(D+I+4)T+u^2]}{\partial x_1}$$
$$=-R_9\hat{f}_9^{(1)}+\hat{A}_9+2\rho u_y\lambda'Q\frac{D+I+2}{D+I}, \tag{54}$$

where $j_x=\rho u_x$, $j_y=\rho u_y$, and $\xi=(D+I)\rho T+(j_x^2+j_y^2)/\rho$ is twice the total energy.

From Eq. (36), we get

$$\frac{\partial\rho}{\partial t_2}=0, \tag{55}$$

$$\frac{\partial j_x}{\partial t_2}+\frac{\partial\hat{f}_5^{(1)}}{\partial x_1}+\frac{\partial\hat{f}_6^{(1)}}{\partial y_1}=0\,, \tag{56}$$

$$\frac{\partial j_y}{\partial t_2}+\frac{\partial\hat{f}_6^{(1)}}{\partial x_1}+\frac{\partial\hat{f}_7^{(1)}}{\partial y_1}=0\,, \tag{57}$$

$$\frac{\partial\xi}{\partial t_2}+\frac{\partial\hat{f}_8^{(1)}}{\partial x_1}+\frac{\partial\hat{f}_9^{(1)}}{\partial y_1}=0\,. \tag{58}$$

Adding Eqs. (46)–(49) and (55)–(58) leads to the following equations:

$$\frac{\partial\rho}{\partial t}+\frac{\partial j_x}{\partial x}+\frac{\partial j_y}{\partial y}=0, \tag{59}$$

$$\frac{\partial j_x}{\partial t}+\frac{\partial\rho\left(T+u_x^2\right)}{\partial x}+\frac{\partial\rho u_xu_y}{\partial y}+\frac{\partial\hat{f}_5^{(1)}}{\partial x}+\frac{\partial\hat{f}_6^{(1)}}{\partial y}=0, \tag{60}$$

$$\frac{\partial j_y}{\partial t}+\frac{\partial\rho u_xu_y}{\partial x}+\frac{\partial\rho\left(T+u_y^2\right)}{\partial y}+\frac{\partial\hat{f}_6^{(1)}}{\partial x}+\frac{\partial\hat{f}_7^{(1)}}{\partial y}=0, \tag{61}$$

$$\frac{\partial\xi}{\partial t}+\frac{\partial\rho u_x[(D+I+2)T+u^2]}{\partial x}+\frac{\partial\rho u_y[(D+I+2)T+u^2]}{\partial y}+\frac{\partial\hat{f}_8^{(1)}}{\partial x}+\frac{\partial\hat{f}_9^{(1)}}{\partial y}=2\rho\lambda'Q. \tag{62}$$

From Eqs. (50)–(54) and (59)–(62), we finally obtain the Navier-Stokes equations:

$$\frac{\partial\rho}{\partial t}+\frac{\partial j_x}{\partial x}+\frac{\partial j_y}{\partial y}=0, \tag{63}$$

$$\frac{\partial j_x}{\partial t}+\frac{\partial\left(p+\rho u_x^2\right)}{\partial x}+\frac{\partial\rho u_xu_y}{\partial y}=\frac{\partial}{\partial x}\left[\frac{\rho T}{R_5}\left(2\frac{\partial u_x}{\partial x}-\frac{2}{D+I}\frac{\partial u_x}{\partial x}-\frac{2}{D+I}\frac{\partial u_y}{\partial y}\right)\right]+\frac{\partial}{\partial y}\left[\frac{\rho T}{R_6}\left(\frac{\partial u_x}{\partial y}+\frac{\partial u_y}{\partial x}\right)\right], \tag{64}$$

$$\frac{\partial j_y}{\partial t}+\frac{\partial\rho u_xu_y}{\partial x}+\frac{\partial\left(p+\rho u_y^2\right)}{\partial y}=\frac{\partial}{\partial x}\left[\frac{\rho T}{R_6}\left(\frac{\partial u_x}{\partial y}+\frac{\partial u_y}{\partial x}\right)\right]+\frac{\partial}{\partial y}\left[\frac{\rho T}{R_7}\left(2\frac{\partial u_y}{\partial y}-\frac{2}{D+I}\frac{\partial u_x}{\partial x}-\frac{2}{D+I}\frac{\partial u_y}{\partial y}\right)\right], \tag{65}$$

$$\frac{\partial\xi}{\partial t}+\frac{\partial(\xi+2p)u_x}{\partial x}+\frac{\partial(\xi+2p)u_y}{\partial y}=2\frac{\partial}{\partial x}\left[\frac{\rho T}{R_8}\left(c_p\frac{\partial T}{\partial x}-\frac{2u_x}{D+I}\frac{\partial u_x}{\partial x}-\frac{2u_x}{D+I}\frac{\partial u_y}{\partial y}+2u_x\frac{\partial u_x}{\partial x}+u_y\frac{\partial u_x}{\partial y}+u_y\frac{\partial u_y}{\partial x}\right)-\frac{1}{2}\frac{\hat{A}_8}{R_8}\right]+2\frac{\partial}{\partial y}\left[\frac{\rho T}{R_9}\left(c_p\frac{\partial T}{\partial y}-\frac{2u_y}{D+I}\frac{\partial u_x}{\partial x}-\frac{2u_y}{D+I}\frac{\partial u_y}{\partial y}+2u_y\frac{\partial u_y}{\partial y}+u_x\frac{\partial u_y}{\partial x}+u_x\frac{\partial u_x}{\partial y}\right)-\frac{1}{2}\frac{\hat{A}_9}{R_9}\right]+2\rho\lambda'Q. \tag{66}$$

Here, $c_p=(D+I+2)/2$ is the specific heat at constant pressure. The specific heat at constant volume can be defined as $c_v=(D+I)/2$. Substituting Eqs. (3) and (4) into the above equation (66) gives

$$\frac{\partial\xi}{\partial t}+\frac{\partial(\xi+2p)u_x}{\partial x}+\frac{\partial(\xi+2p)u_y}{\partial y}=2\frac{\partial}{\partial x}\left[c_p\frac{\rho T}{R_8}\frac{\partial T}{\partial x}+\frac{\rho T}{R_5}\left(-\frac{2u_x}{D+I}\frac{\partial u_x}{\partial x}-\frac{2u_x}{D+I}\frac{\partial u_y}{\partial y}+2u_x\frac{\partial u_x}{\partial x}+u_y\frac{\partial u_x}{\partial y}+u_y\frac{\partial u_y}{\partial x}\right)\right]+2\frac{\partial}{\partial y}\left[c_p\frac{\rho T}{R_9}\frac{\partial T}{\partial y}+\frac{\rho T}{R_7}\left(-\frac{2u_y}{D+I}\frac{\partial u_x}{\partial x}-\frac{2u_y}{D+I}\frac{\partial u_y}{\partial y}+2u_y\frac{\partial u_y}{\partial y}+u_x\frac{\partial u_y}{\partial x}+u_x\frac{\partial u_x}{\partial y}\right)\right]+2\rho\lambda'Q, \tag{67}$$

It is clear to find that, by substituting the specific form of $\hat{A}_8$ and $\hat{A}_9$ into Eq. (66), the viscous coefficient in the energy equation (67) is consistent with that in the momentum equation (65). Up to this step, we can find that the proposed MRT-LBKM recover the consistent Navier-Stokes equations in the hydrodynamic limit.

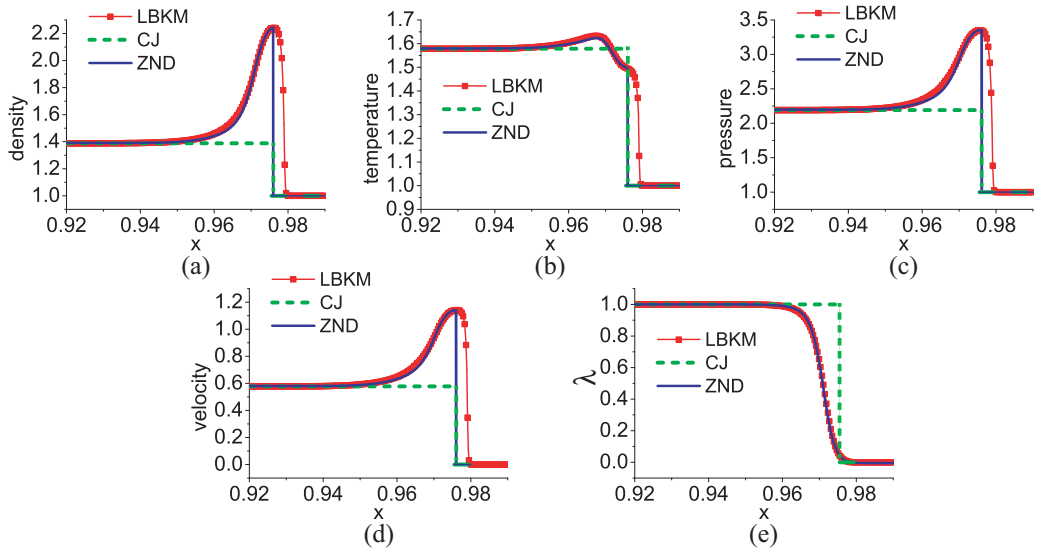


FIG. 2. (Color online) The profiles of the steady detonation: (a) $\rho$, (b) $T$, (c) $p$, (d) $u_x$, (e) $\lambda$.

More discussions are as follows. The coefficient $\hat{\mathbf{R}}$ represents the inverse of the relaxation time from $\hat{\mathbf{f}}$ to its equilibrium $\hat{\mathbf{f}}^{\mathbf{eq}}$. $\hat{f}_1 = \hat{f}_1^{eq}$, $\hat{f}_2 = \hat{f}_2^{eq}$, $\hat{f}_3 = \hat{f}_3^{eq}$, $\hat{f}_4 = \hat{f}_4^{eq}$. Consequently, the values of $R_1$, $R_2$, $R_3$, $R_4$ have no influence on the LB evolution. Furthermore, the relaxation parameters $R_i$ are not completely independent for the system with isotropy constraints [74]. Specifically, $R_5$, $R_6$, $R_7$ are related to viscosity, and the viscosity coefficient is $\mu = \rho T/R_\mu$ when $R_5 = R_6 = R_7 = R_\mu$; $R_8$, $R_9$ are related to heat conductivity, and the heat conductivity coefficient is $\kappa = c_p \rho T/R_\kappa$ when $R_8 = R_9 = R_\kappa$. Consequently, both the specific-heat ratio

$$\gamma = \frac{c_p}{c_v} = \frac{D+I+2}{D+I}, \tag{68}$$

and the Prandtl number,

$$\mathrm{Pr} = \frac{c_p \mu}{\kappa} = \frac{R_\kappa}{R_\mu}, \tag{69}$$

are flexible in this model. When $R_5 = R_6 = R_7 = R_\mu$, $R_8 = R_9 = R_\kappa$, the above Navier-Stokes equations reduce to

$$\frac{\partial \rho}{\partial t} + \frac{\partial j_\alpha}{\partial r_\alpha} = 0, \tag{70}$$

$$\frac{\partial j_\alpha}{\partial t} + \frac{\partial p}{\partial r_\alpha} + \frac{\partial \rho u_\alpha u_\beta}{\partial r_\beta} = -\frac{\partial P_{\alpha\beta}}{\partial r_\beta}, \tag{71}$$

$$\frac{\partial \xi}{\partial t} + \frac{\partial (\xi + 2p) u_\alpha}{\partial r_\alpha} = 2\rho\lambda' Q + 2\frac{\partial}{\partial r_\beta}\left(\kappa \frac{\partial T}{\partial r_\beta} - P_{\alpha\beta} u_\alpha\right), \tag{72}$$

where

$$\mu_B = \mu\left(\frac{2}{3} - \frac{2}{D+I}\right), \tag{73}$$

$$P_{\alpha\beta} = -\mu\left(\frac{\partial u_\alpha}{\partial r_\beta} + \frac{\partial u_\beta}{\partial r_\alpha} - \frac{2}{3}\frac{\partial u_\chi}{\partial r_\chi}\delta_{\alpha\beta}\right) - \mu_B \frac{\partial u_\chi}{\partial r_\chi}\delta_{\alpha\beta}. \tag{74}$$

Specifically, $P_{xx} = \hat{f}_5^{(1)}$, $P_{xy} = P_{yx} = \hat{f}_6^{(1)}$, $P_{yy} = \hat{f}_7^{(1)}$.

## IV. NUMERICAL TESTS OF THE MODEL

To validate and verify the proposed LBKM, here we show simulation results of some well-known benchmark numerical examples which include one for the steady detonation, three for the Riemann problems, one for the shock reflection, and one for the Couette flow. The parameter for chemical reaction heat $Q$ is not zero only for the first numerical test. For the cases with the Couette flow, results with different specific-heat ratios and Prandtl numbers are shown.

### A. Steady detonation

As the first numerical test, a one-dimensional steady detonation is simulated here to validate our model. The initial physical quantities are

$$\begin{aligned}(\rho, T, u_x, u_y, \lambda)_L &= (1.38837, 1.57856, 0.577350, 0, 1),\\ (\rho, T, u_x, u_y, \lambda)_R &= (1, 1, 0, 0, 0),\end{aligned} \tag{75}$$

where the suffixes $L$ and $R$ index two parts, $0 \leqslant x \leqslant 0.2$ and $0.2 < r \leqslant 1$, respectively. Here we choose $v_a = 2.7$, $v_b = 2.2$, $v_c = 1.2$, $\eta_a = 5$, $\eta_b = 3$, $\eta_c = 1.1$, $I = 3$, $\Delta t = 5 \times 10^{-6}$, $\Delta x = \Delta y = 2 \times 10^{-4}$, $Q = 1$. The collision parameters in MRT are $R_5 = R_6 = R_7 = 10^4$ and $10^5$ for the others. Figure 2 shows the profile of the steady detonation at time $t = 0.39$. Figures 2(a)–2(e) give physical quantities $\rho$, $T$, $p$, $u_x$, $\lambda$ versus $x$, respectively. The simulation results of LBKM, analytic solutions of Chapman-Jouguet (CJ) theory [18,19,23], and Zeldovich-Neumann-Doering (ZND) theory [20–23] are shown in each panel. The solid lines with squares, the dashed lines, and the solid lines are for LBKM simulation results, CJ results, and ZND results, respectively. The simulation results give physical quantities behind the detonation wave $(\rho, T, u_x, u_\theta, \lambda) = (1.38869, 1.57816, 0.577384, 0, 1)$. Comparing them with CJ results gives the relative differences 0.023%, 0.025%, 0.006%, 0%, and 0%, respectively. It is clear in Figs. 2(a)–2(e) that the LBKM simulation results agree well with the ZND results in the area behind von Neumann peak. But, there exist significant differences in front of the

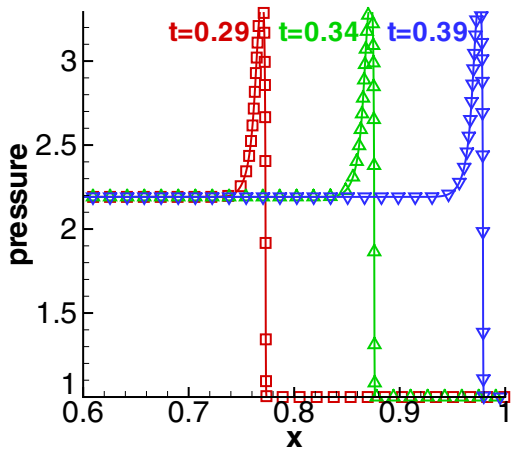


FIG. 3. (Color online) The profiles of $p$ in the evolution of the steady detonation at times $t = 0.29, 0.34, 0.39$, respectively.

von Neumann peaks. This is because the ZND theory used here ignores completely the effects of viscosity and heat conduction, and the von Neumann peak is treated simply as a strong discontinuity which is not true. While in the LBKM results the effects of viscosity, heat conduction, and other kinds of relevant transportation are included. This difference will decrease with the decreasing of viscosity and heat conductivity. This point will be further discussed in Sec. VI.

Figure 3 shows the pressure versus $x$ at times $t = 0.29$, 0.34, 0.39, from left to right, respectively. Our simulation gives detonation velocity $v_D = 2.06$, and the analytic solution is $v_D = 2.06395$. The relative difference between them is 0.191% which is satisfying.

### B. Riemann problems

In this section, our two-dimensional LBKM is used to solve the one-dimensional Riemann problems where there is no chemical reaction. Now, we give simulation results for three typical Riemann problems, i.e., the Sod's shock tube, the Lax's shock tube, and the Sjogreen's problem.

#### 1. Sod's shock tube

For the problem of Sod's shock tube, the initial condition is described by

$$\begin{aligned}(\rho,T,u_x,u_y)_L &= (1,1,0,0),\\ (\rho,T,u_x,u_y)_R &= (0.125,0.8,0,0),\end{aligned} \tag{76}$$

where left side $L \in [0,0.5)$ and the right side $R \in [0.5,1]$. Figure 4 shows the computed density, temperature, pressure, velocity profiles at the time $t = 0.2$. The lines are for analytical solutions and solid lines with squares are for the LB simulation results. The size of grid is $\Delta x = \Delta y = 10^{-3}$, time step $\Delta t = 10^{-5}$, $I = 3$, and $(v_a, v_b, v_c, \eta_a, \eta_b, \eta_c) = (2.5, 2.2, 1.2, 6.5, 3, 0)$. The collision parameters in MRT are $R_5 = R_6 = R_7 = 1.2 \times 10^4$, and other values of $R_i$ are $10^5$. It is easy to find in Fig. 4 that the two sets of results have a satisfying agreement.

#### 2. Lax's shock tube

For this problem, the initial condition is described by

$$\begin{aligned}(\rho,T,u_x,u_y)_L &= (0.445,7.928,0.698,0),\\ (\rho,T,u_x,u_y)_R &= (0.5,1.142,0,0),\end{aligned} \tag{77}$$

where $L \in [-1,0)$ and $R \in [0,1]$. Figure 5 shows the physical quantities (density, temperature, pressure, velocity) versus $x$ at the time $t = 0.15$. The lines are for exact solutions and solid lines with squares correspond to our simulation results. The parameters are set to be $\Delta x = \Delta y = 10^{-3}$, $\Delta t = 10^{-5}$, $I = 1$, $(v_a, v_b, v_c, \eta_a, \eta_b, \eta_c) = (4.7, 3.3, 1, 6, 2.5, 0.9)$. The collision parameters in MRT are $R_5 = R_6 = R_7 = 2 \times 10^4$, $R_8 = R_9 = 8 \times 10^4$, and other values of $R_i$ are $10^5$. We also find a good agreement between the exact solutions and our simulation results.

#### 3. Sjogreen's problem

The initial condition for the Sjogreen's problem is

$$\begin{aligned}(\rho,T,u_x,u_y)_L &= (1.0,0.5,-1.2,0),\\ (\rho,T,u_x,u_y)_R &= (1.0,0.5,1.2,0),\end{aligned} \tag{78}$$

where $L \in [-0.5,0)$ and $R \in [0,0.5]$. Figure 6 shows the physical quantities versus $x$ at the time $t = 0.03$. The specific correspondences are referred to the legends. The parameters used here are $\Delta x = \Delta y = 2 \times 10^{-3}$, $\Delta t = 2 \times 10^{-5}$, $I = 4$, $(v_a, v_b, v_c, \eta_a, \eta_b, \eta_c) = (0.4, 1.0, 1.8, 0.3, 1.9, 1.5)$. The collision parameters in MRT are $R_8 = R_9 = 2 \times 10^4$, and others $5 \times 10^4$. We also find a good agreement between the two sets of results.

### C. Shock reflection

Shock reflection problem, which has been the subject of considerable research effort over the last seven decades, is one of the most important problems in both the science and engineering fields. Of particular interest is, in general,

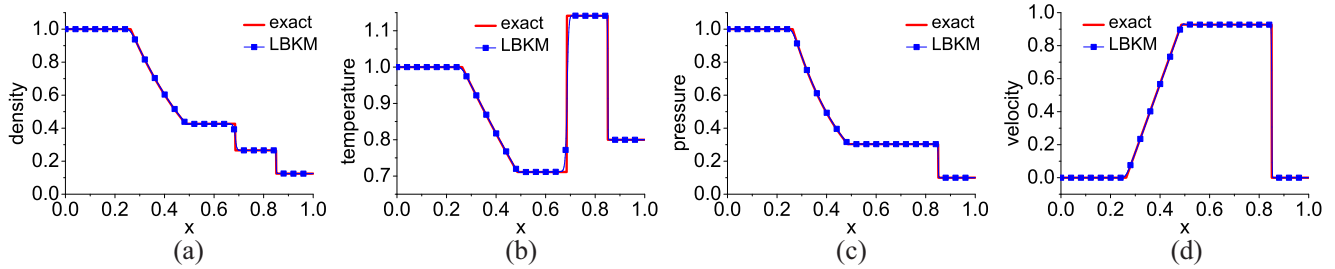


FIG. 4. (Color online) Comparison of numerical and theoretical results for the Sod shock tube at $t = 0.2$. Solid lines are for exact solutions and solid lines with squares are for simulation results.

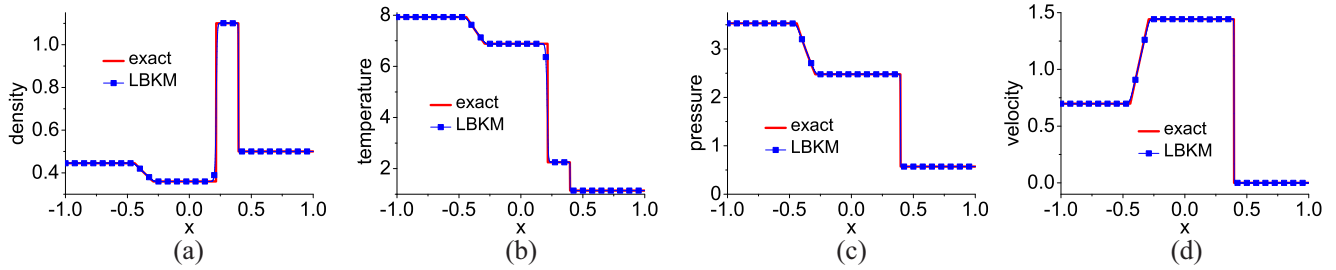


FIG. 5. (Color online) Comparison of numerical and theoretical results for the Lax shock tube at $t = 0.15$. Solid lines are for exact solutions and solid lines with squares are for simulation results.

the transition from so-called regular to irregular reflection. Consider a plane shock (for example, one generated by a wedge in steady inviscid flow) being reflected off a wall, as schematically shown in Fig. 7(a). The type of reflection depends on $(M_1, \gamma, \theta)$ parameter space, where $M_1$, $\gamma$, and $\theta$ are the incident shock wave Mach number, gas specific-heat ratio, and flow deflection angle, respectively. In regular reflection, the incident shock wave ($I$) and the reflected shock wave ($R$) meet at the surface and are typical for a large wall angle $\phi$. In the case of regular reflection, the conservations of mass, momentum, and energy relate the state downstream of the shock (subscript 2) to the state upstream (subscript 1) as follows:

$$\frac{\rho_2}{\rho_1} = \frac{(\gamma+1)M_1^2 \sin^2\phi}{2+(\gamma-1)M_1^2 \sin^2\phi}, \tag{79}$$

$$\frac{p_2}{p_1} = \frac{2\gamma M_1^2 \sin^2\phi - (\gamma-1)}{\gamma+1}, \tag{80}$$

$$M_2 \sin^2(\phi-\theta) = \frac{\gamma+1+(\gamma-1)\left(M_1^2\sin^2\phi-1\right)}{\gamma+1+2\gamma\left(M_1^2\sin^2\phi-1\right)}, \tag{81}$$

$$\tan\theta = \frac{\tan\phi\left(M_1^2\cos^2\phi-\cot^2\phi\right)}{1+\frac{1}{2}M_1^2(\gamma+\cos 2\phi)}. \tag{82}$$

For fixed $\gamma$ and $M_1$, the shock angle $\phi$ behaves as a function of the deflection angle $\theta$.

Here, we show a numerical test as follows. An incoming shock wave with Mach number $M_1 = 2.3094$ has an angle of $\phi = 30^\circ$ to the wall. The computational domain is a rectangle with length 0.3 and height 0.1. This domain is divided into a $300 \times 100$ rectangular grid with $\Delta x = \Delta y = 10^{-3}$. The boundary conditions are composed of a reflecting surface along the bottom boundary, supersonic outflow along the right boundary, and Dirichlet conditions on the left and top boundary conditions, given by

$$\begin{aligned}(\rho,T,u_x,u_y)_{0,y,t} &= (1,0.5,2,0),\\ (\rho,T,u_x,u_y)_{x,0.1,t} &= (1.25,0.56,1.9,-0.173205).\end{aligned} \tag{83}$$

The parameters are chosen as $\Delta t = 5\times10^{-6}$, $I = 2$ ($\gamma = 1.5$), $(v_a,\ v_b,\ v_c,\ \eta_a,\ \eta_b,\ \eta_c) = (1.0,\ 2.7,\ 2.9,\ 1.0,\ 2.9,\ 0.96)$. The collision parameters in MRT are $R_5 = R_6 = R_7 = 1.8\times10^5$, $R_8 = R_9 = 2.0\times10^5$, and other values of $R_i$ are $10^5$. Figure 7(b) shows contours of density at $t = 0.5$. The clear shock reflection on the wall agrees well with the exact solution. [For example, from the boundary conditions, especially the bottom boundary condition shown by the second equation in Eq. (83), we obtain $\tan\theta = 0.173205/1.9$. If substitute the values of $\phi$, $M_1$, $\gamma$ into Eq. (82), we get exactly the same value for $\tan\theta$, $9.1161\times10^{-2}$, if we calculate in single precision.]

### D. Couette flow

In order to demonstrate that the model is also suitable for incompressible flows, we conduct a series of numerical simulations of Couette flow. The upper wall, with the distance $H = 0.2$ apart from the lower wall, moves with a fixed speed $u_0$. The lower wall is at rest. Periodic boundary conditions are applied to the left and right boundaries, and the top and bottom adopt the nonequilibrium extrapolation method.

In the first simulation of Couette flow, the initial state of the fluid is $\rho = 1$, $T = 1$, $u_x = u_y = 0$. The viscous shear stress transmits momentum into the fluid and changes the horizontal speed profile [73]. Figure 8 shows the horizontal speed distribution at various instants $t = 1$, 5, 30. The simulation

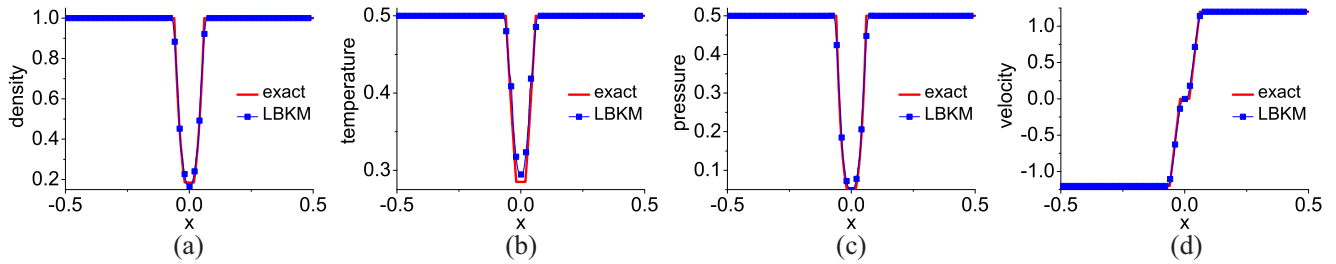


FIG. 6. (Color online) Comparison of numerical and theoretical results for the Sjogreen's problem at $t = 0.03$. Solid lines are for exact solutions and solid lines with squares are for simulation results.

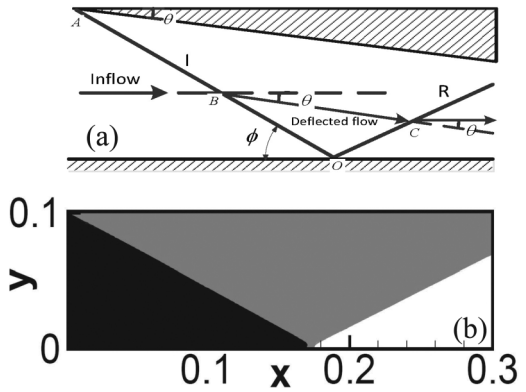


FIG. 7. Schematic (a) and density contour (b) of steady regular shock reflection on a wall. In (b), from black to white, the density increases.

results coincide well with the following analysis:

$$u = \frac{y}{H}u_0 + \frac{2}{\pi}u_0\sum_{n=1}^{\infty}\left[\frac{(-1)^n}{n}\exp\left(-n^2\pi^2\frac{\mu t}{\rho H^2}\right)\times\sin\left(\frac{n\pi y}{H}\right)\right]. \quad (84)$$

The parameters are $\Delta x = 10^{-3}$, $\Delta t = 10^{-5}$, $I = 2$, $(v_a, v_b, v_c, \eta_a, \eta_b, \eta_c) = (0.8, 1.2, 1.3, 1.0, 2.7, 0.8)$. The grid number is $N_x \times N_y = 1 \times 200$. The collision parameters are $R_5 = R_6 = R_7 = 2 \times 10^3$, $R_8 = R_9 = 1.0 \times 10^4$, and the others $5 \times 10^4$.

Figure 9 shows the temperature profiles in another four simulations. In order to get a steady fluid state as soon as possible, we give the initial temperature field as follows:

$$T = T_1 + (T_2 - T_1)\frac{x}{H} + \frac{\mu}{2\kappa}u_0^2\frac{x}{H}\left(1 - \frac{x}{H}\right), \quad (85)$$

where $T_1$ (=1.0) and $T_2$ (=1.01) are temperatures of the lower and upper walls, respectively. The initial velocity field is given as $u = u_0 y/H$. And the time is $t = 0.01$. Figures 9(a) and 9(b) correspond to $\gamma = 1.4$ and 1.5, respectively. The case Pr = 0.2 in Fig. 9(a) corresponds to $\Delta x = 10^{-3}$, $\Delta t = 10^{-5}$, $I = 3$, $v_a = 0.8$, $v_b = 1.2$, $v_c = 1.3$, $\eta_a = 1.1$, $\eta_b = 3.1$, $\eta_c = 0.7$, $R_5 = R_6 = R_7 = 10^4$, $R_8 = R_9 = 2 \times 10^3$, $R_{21} = R_{22} = R_{23} = R_{24} = 10^3$, and $5 \times 10^4$ for other collision parameters. For the case Pr = 5.0 in Fig. 9(a), the parameters are

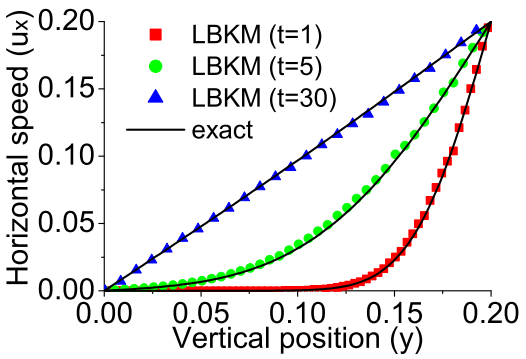


FIG. 8. (Color online) Horizontal speed distribution of Couette flow at various instants: $t = 1$, 5, and 30.

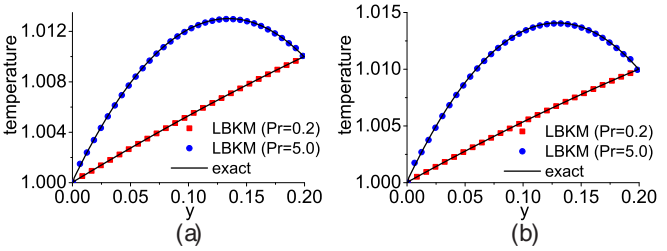


FIG. 9. (Color online) Temperature profiles of Couette flow. (a) $\gamma = 1.4$. (b) $\gamma = 1.5$.

$\eta_c = 0.7$, $R_5 = R_6 = R_7 = 2 \times 10^3$, $R_8 = R_9 = 10^4$, $R_{21} = R_{22} = R_{23} = R_{24} = 5 \times 10^4$, and the others are the same as those for Pr = 0.2 in Fig. 9(a). Except $I = 2$ and $\eta_b = 2.1$, all the other parameters for the cases Pr = 0.2 and Pr = 5.0 in Fig. 9(b) are the same as those for the cases Pr = 0.2 and Pr = 5.0 in Fig. 9(a), respectively. It is clear that our simulation results are in agreement with the analytical ones, and the effects of the specific-heat ratio and the Prandtl number are successfully captured.

The analytical solutions used in the shock tube and shock reflection problems are based on the Euler equations. The numerical tests show that, by using large collision parameters (small viscosity and heat conductivity, etc.), the LBKM can present results having a satisfying agreement with those based on the Euler equations. The analytical solutions used in the Couette flow problems are based on the Navier-Stokes equations. The numerical tests show that the LBKM can present results having a satisfying agreement with those of Navier-Stokes equations.

## V. PHYSICAL GAINS AND COMPUTING COSTS

We first discuss the computational costs for the MRT and SRT versions of LBKM based on the same discrete velocity model. In 2013, we proposed a uniform scheme for formulating LBKM [76]. In this work, we formulate the discrete velocity model according to the same idea. In this scheme, we first check which moment relations of $f^{eq}$ are needed to recover the hydrodynamic equations. Those moment relations can be written in the uniform form

$$\mathbf{M}\mathbf{f}^{eq} = \hat{\mathbf{f}}^{eq}, \quad (86)$$

where $\mathbf{M}$ is $N \times N$ matrix, $N$ is an integer to be fixed in the next step. We rewrite the above moment relations in the explicit Cartesian coordinates and check the equation number which is the value of $N$ . In this way we can find the minimum number $N$ of needed discrete velocities. This scheme works for both the MRT-LBKM and SRT-LBKM formulations. In this formulation scheme, we can roughly estimate the computational costs of the MRT and SRT versions as in the following.

The SRT and MRT versions of LB kinetic equations read as

$$\frac{\partial f_i}{\partial t} + v_{i\alpha}\frac{\partial f_i}{\partial r_\alpha} = -\frac{1}{\tau}\left(f_i - M_{il}^{-1}\hat{f}_k^{eq}\right) + C_i \quad (87)$$

TABLE I. Computing times for simulating a steady detonation process using various versions of the LBKM.

| Model | Computing time (unit: s) |
|---|---|
| MRT D2V24 | 2293.93 |
| SRT D2V24 | 2221.58 |
| SRT D2V33 | 2461.58 |

and

$$\frac{\partial f_i}{\partial t} + v_{i\alpha}\frac{\partial f_i}{\partial r_\alpha} = -M_{il}^{-1}\left[\hat{R}_{lk}\left(\hat{f}_k - \hat{f}_k^{eq}\right) + \hat{A}_l\right] + C_i, \quad (88)$$

respectively. Compared with the SRT version, the extra computation cost of MRT includes two parts: the first part is for computing $\hat{f}_k = M_{ki} f_i$, the second is for $\hat{A}_l$ which has only two nonzero terms. As mentioned in Sec. II, an important skill here is that the inverse of the matrix $\mathbf{M}$ should be solved analytically before coding. We use the software MATLAB2011 to do this. Thus, the elements of $\mathbf{M}^{-1}$ have been replaced by specific values before the main loop of the simulation, instead of being numerically solved in each iteration step.

To have a rough estimation on the computing time, we performed simulations of the same physical processes by using various LB models. The computational facility is a personal computer with Intel(R) Core(TM) 2 CPU Q9400 @2.66 GHz and RAM 4.00 GB. Table I shows the computing times for three LBKM simulations of the same steady detonation behavior. The first simulation in Table I is actually the first numerical test in Fig. 2. It is performed using the current MRT-LBKM with 24 discrete velocities in Eq. (88). The second is performed using the SRT-LBKM [Eq. (87)] with the same D2V24, where the relaxation time is chosen as $\tau = 10^{-5}$, and the other parameters are chosen as the same as in the first simulation. The third is performed using the SRT-LBKM described by the following equation:

$$\frac{\partial f_i}{\partial t} + v_{i\alpha}\frac{\partial f_i}{\partial r_\alpha} = -\frac{1}{\tau}\left(f_i - f_i^{eq}\right) + C_i, \quad (89)$$

with the D2V33 by Watari [73] where 33 discrete velocities are used. Since the D2V33 works only for the case where the specific-heat ratio is fixed at $\gamma = 2$, the parameter $I = 0$ is used in the third simulation, which does not influence the computing time. It is easy to find that the computing time for the simulation using the current MRT is only 3% more than that using the SRT with the same DVM, and is 7% less than that using the SRT with DVM with 33 discrete velocities.

It is interesting to have some comments on the MRT-LBKM versus the Navier-Stokes model.

(1) The two-dimensional Navier-Stokes model is composed of 4 nonlinear partial differential equations. The current two-dimensional LBKM contains 24 (formally) linear equations.

(2) The linearity of the LB kinetic equations makes easy the algorithm and coding. But the larger number of equations increase the computational cost. If we are only interested in the density $\rho$, the momentum $\rho\mathbf{u}$ and the energy $E$, from which the flow velocity $\mathbf{u}$, temperature $T$ can be obtained and then the pressure $p$ can also be obtained from the equation of state, the Navier-Stokes model may be more efficient if without considering parallel computing.

(3) It is understandable that a lower-cost model is generally preferable. A higher-cost model shows its necessity to be developed only in the following two cases: (a) it can bring more information from which one can gain a more complete or deeper insight into the problem under consideration, or (b) it can bring more accurate results for the physical quantities under consideration.

Physically, the proposed LBKM is roughly equivalent with a Navier-Stokes model supplemented by a coarse-grained model of the TNE behaviors in the continuum limit. The two-dimensional Navier-Stokes model describes the behaviors of the 4 quantities $\rho$, $\rho u_x$, $\rho u_y$, and $\xi$, which are conserved in the collision process. The 20 physical quantities $\hat{f}_k - \hat{f}_k^{eq}$ (with $k = 5, 6, \ldots, 24$ ) constitute a rough description on the TNE behaviors. The conserved and nonconserved quantities are complementary in describing more completely the behaviors of complex flows. So, the LBKM proposed in the work belongs to the above case (a).

As for case (b), by using the idea shown in this paper, it is straightforward to construct a LBKM which can bring more accurate values of $\rho$, $\rho u_x$, $\rho u_y$, and $\xi$ than the Navier-Stokes model in the case or region where the local Knudsen number $\varepsilon$ is high, for example, around strong shock and detonation waves or when the flow behavior under consideration is much faster than the case considered in this work. To that aim, we need only use a different DVM constructed according to a longer list of moment relations of $f^{eq}$. To save the computational cost, we can prepare several, at least two, DVMs in the code. The DVM can be chosen adaptively according to the local Knudsen number $\varepsilon$. For example, when the local Knudsen number $\varepsilon$ is higher than the case where the Navier-Stokes model works, the code will adaptively use a different DVM with more discrete velocities. When the local Knudsen number $\varepsilon$ is smaller than some critical value, the code will adaptively use a DVM with fewer discrete velocities. A coarse-grained modeling or approximation $f_i = f_i^{eq}$ can be used at the first iteration step after switching to a different DVM. The careful discussion on LBKM with flexible DVMs is out of the scope of the paper.

(4) One can always obtain the evolution equations of the nonconserved quantities via the Chapman-Enskog analysis to the Boltzmann equation, which is independent of the LBKM. That is to say, without LBKM, one can also solve the coupled 24 evolution equations of conserved and nonconserved physical quantities using the traditional CFD scheme. But, solving the coupled 24 nonlinear partial differential equations is not an easy task. The 24 LB kinetic equations are (formally) linear and have the same form. The computations in LBKM are easy to be parallelized. In brief, when one aims to investigate both the HNE and TNE behaviors, the LBKM is a convenient model.

## VI. NONEQUILIBRIUM INVESTIGATION OF DETONATION

The LB kinetic model inherits naturally the function of Boltzmann equation, describing nonequilibrium effects in the system [33,44,68,76–79]. The departure of the system from

local thermodynamic nonequilibrium can be roughly measured by the difference between the high order kinetic moments of $f_i$ and $f_i^{eq}$ which are just $(\hat{f}_k - \hat{f}_k^{eq})$ in the current MRT-LB kinetic equation (1). We define

$$\Delta_k = \hat{f}_k - \hat{f}_k^{eq}. \tag{90}$$

It is easy to find that $\Delta_k = 0$ for $k = 1, 2, 3, 4$ due to the conservation of mass, momentum, and energy. Each nonzero $\Delta_k$ quantitatively describes the deviation status of the system from its local thermodynamic equilibrium from its own side. We can observe the thermodynamic nonequilibrium state in the $N$-dimensional space opened by $\Delta_k$ with $k = 1, 2, \ldots, N$. We further define a distance

$$d = \sqrt{\sum_1^N \Delta_k^2}, \tag{91}$$

which is a rough and averaged estimation of the deviation amplitude from the thermodynamic equilibrium, where $\Delta_k$ is assumed to be dimensionless. Thus, $d = 0$ when the system is in the thermodynamic equilibrium and $d > 0$ in the thermodynamic nonequilibrium state.

In this part, we give some results of $\Delta_k$ in the evolution of detonation. Corresponding to the simple definition of $\Delta_k$, we introduce some clear symbols as $\Delta_{v_x v_x} = \Delta_5$, $\Delta_{v_x v_y} = \Delta_6$, $\Delta_{v_y v_y} = \Delta_7$, $\Delta_{\eta^2} = \Delta_4 - \Delta_5 - \Delta_7$, $\Delta_{(v^2+\eta^2)v_x} = \Delta_8$, $\Delta_{(v^2+\eta^2)v_y} = \Delta_9$, $\Delta_{v_x v_x v_x} = \Delta_{10}$, $\Delta_{v_x v_x v_y} = \Delta_{11}$, $\Delta_{v_x v_y v_y} = \Delta_{12}$, $\Delta_{v_y v_y v_y} = \Delta_{13}$.

A short discussion is as follows. The nonequilibrium behaviors of various modes may contribute to the system evolution according to different amplification factors $R_k$, while all the amplification factors becomes the same in the SRT-LB model. Mathematically, the part $R_k \Delta_k$ in the right side of Eq. (29) increases with increasing $R_k$ for fixed $\Delta_k$.

In this section, we first investigate the unsteady detonation, then compare the cases where the detonation changes from unsteady to steady. All these cases show complex interplay between various HNE behaviors, between various TNE behaviors, and between the HNE and TNE behaviors.

### A. Unsteady detonation: Simulations with different space and time steps

Now, we investigate some nonequilibrium behaviors in detonation phenomena. The initial physical quantities $(\rho, T, u_x, u_y, \lambda)$ are given the same values as those in Eq. (75). Here we choose $v_a = 2.7$, $v_b = 2.2$, $v_c = 1.2$, $\eta_a = 1.5$, $\eta_b = 0.5$, $\eta_c = 5.0$, $I = 3$, $Q = 1$. The collision parameters in MRT are $R_i = 100$. In numerical simulations, the space and time steps should be small enough so that the spurious transportation behaviors are negligible compared with the physical ones. To assure that the numerical errors are small enough, we simulate the same detonation behavior using three sets of spatial and temporal steps: (i) $\Delta x = \Delta y = 10^{-3}$, $\Delta t = 10^{-5}$; (ii) $\Delta x = \Delta y = 10^{-3}$, $\Delta t = 10^{-6}$; (iii) $\Delta x = \Delta y = 10^{-4}$, $\Delta t = 10^{-6}$.

Figure 10 shows the simulation results of physical quantities ($\rho$, $T$, $p$, $u_x$, $\lambda$, $\Delta_{v_x v_x}$, $\Delta_{v_x v_y}$, $\Delta_{v_y v_y}$, $\Delta_{\eta^2}$, $\Delta_{v_x v_x v_x}$, $\Delta_{v_x v_x v_y}$, $\Delta_{v_x v_y v_y}$, $\Delta_{v_y v_y v_y}$, $\Delta_{(v^2+\eta^2)v_x}$, $\Delta_{(v^2+\eta^2)v_y}$) versus $x$ at time $t = 0.35$ in the three cases. A vertical dashed guideline is plotted in each panel to guide the eye for the horizontal position $x = 0.8345$ corresponding to the peak of pressure. It should be pointed out that up to this time the detonation has not obtained its steady state. The pressure at the von Neumann peak will increase further. We choose such a time because it is interesting to study the complex interplay between various nonequilibrium behaviors in the unsteady detonation process:

(1) At the same time, $t = 0.35$, the detonation shown in Fig. 3 has already been steady, but the current one has not. The physical reason is that the viscosity of the system here is much larger than that shown in Fig. 3. It takes more time for the steady detonation wave to form.

(2) All the simulation results in Figs. 10(a)–10(o) are physically reasonable. The simulation results of each quantity in the three cases have a satisfying coincidence. It shows that the grid size 0.001 and the time step $10^{-5}$ are small enough for the current problem. Given $R_i$ small enough, the physical viscosity is much larger than numerical viscosity here.

(3) Figures 10(a)–10(e) show that the maximum values of density, temperature, pressure, velocity are not located at the same $x$ coordinate, and the pressure peak is located in the reaction zone where $0 < \lambda < 1$. It shows that, before the reaction finishes, the temperature first arrives at its peak value, then the pressure, density, and flow velocity arrive at their peak values. Here, we refer to the von Neumann peak as the point where the pressure has its largest value. When the reaction finishes, all the density, temperature, pressure, and the flow velocity have passed their peak values.

(4) As shown in Figs. 10(f), 10(h), and 10(i), the simulation results of $\Delta_{v_x v_x}$, $\Delta_{v_y v_y}$, and $\Delta_{\eta^2}$ satisfy the relation $\Delta_{v_x v_x} + \Delta_{v_y v_y} + \Delta_{\eta^2} = 0$. Here, what $\Delta_{v_x v_x}$, $\Delta_{v_y v_y}$, and $\Delta_{\eta^2}$ describe are the departures of the internal energies in the $x$, $y$, and extra degrees of freedom from their average. The relaxation coefficients $R_5$ and $R_7$ are related to evolution speeds of the internal energies in $x$ and $y$ degrees of freedom, respectively. This result is physically reasonable. The results in Figs. 10(f), 10(h), and 10(i) show clearly that, when the system is not in its thermodynamic equilibrium state, the internal energies in different degrees of freedom may not equal each other, that the exchange of the internal energies in different degrees of freedom, due to the molecule collision, makes them evolve towards their average.

(5) Both $\Delta_{v_x v_x}$ and $\Delta_{\eta^2}$ show a crest and a trough in the reaction zone, while $\Delta_{v_y v_y}$ shows a crest and two troughs. The result of $\Delta_{v_x v_x}$ first shows a crest and then a trough when the detonation wave travels forward, while $\Delta_{\eta^2}$ show an opposite behavior. The crest of $\Delta_{v_y v_y}$ is in-between its two troughs. Physically, comparing with the internal energy in the $y$ or extra degree of freedom, the internal energy in the $x$ degree of freedom first increases in the preshocked area. The maximum absolute value of $\Delta_{v_x v_x}$ is the largest among $\Delta_{v_x v_x}$, $\Delta_{v_y v_y}$, and $\Delta_{\eta^2}$ in the whole range shown in the figure.

(6) Figures 10(g), 10(k), 10(m), and 10(o) show that the results of $\Delta_{v_x v_y}$, $\Delta_{v_x v_x v_y}$, $\Delta_{v_y v_y v_y}$, $\Delta_{(v^2+\eta^2)v_y}$ are equal to zero. Here, $\Delta_{v_x v_y}$ associates with the shear effect, $\Delta_{v_x v_x v_y}$, $\Delta_{v_y v_y v_y}$, $\Delta_{(v^2+\eta^2)v_y}$ are related to "the internal energy flow caused by microscopic fluctuation" in the $y$ direction. The results are consistent with the fact that the simulated system is one dimensional or uniformly symmetric in the $y$ direction. There is neither shear effect nor energy flux in the $y$ direction.

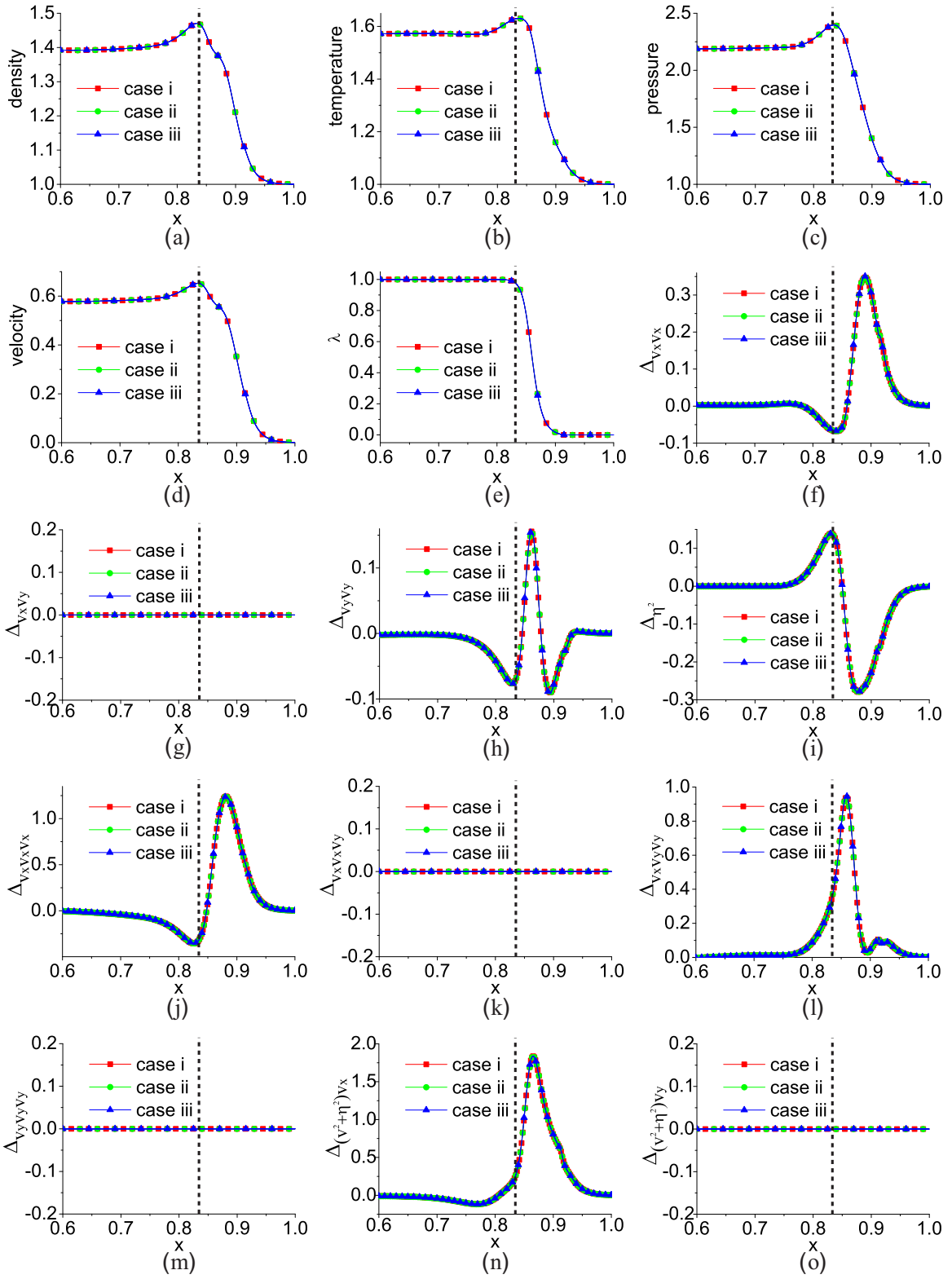


FIG. 10. (Color online) Physical quantities versus $x$ at time $t = 0.35$ in three cases: (a) $\rho$, (b) $T$, (c) $p$, (d) $u_x$, (e) $\lambda$, (f) $\Delta_{v_x v_x}$, (g) $\Delta_{v_x v_y}$, (h) $\Delta_{v_y v_y}$, (i) $\Delta_{\eta^2}$, (j) $\Delta_{v_x v_x v_x}$, (k) $\Delta_{v_x v_x v_y}$, (l) $\Delta_{v_x v_y v_y}$, (m) $\Delta_{v_y v_y v_y}$, (n) $\Delta_{(v^2+\eta^2)v_x}$, (o) $\Delta_{(v^2+\eta^2)v_y}$.

(7) It can be found in Figs. 10(j), 10(l), and 10(n) that $\Delta_{v_x v_x v_x}$, $\Delta_{v_x v_y v_y}$, $\Delta_{(v^2+\eta^2)v_x}$ deviate significantly from zero. $\Delta_{v_x v_x v_x}$, $\Delta_{v_x v_y v_y}$, $\Delta_{(v^2+\eta^2)v_x}$ are associated with "the internal energy flow caused by microscopic fluctuation" in the $x$ direction. As the chemical energy is released continuously in the reaction zone, the compression and rarefaction make effects on the system successively, Those actions make the velocity distribution function asymmetrical about the point $(v_x = u_x,\ v_y = u_y)$ which is the symcenter of the Maxwellian distribution [see Eq. (21)].

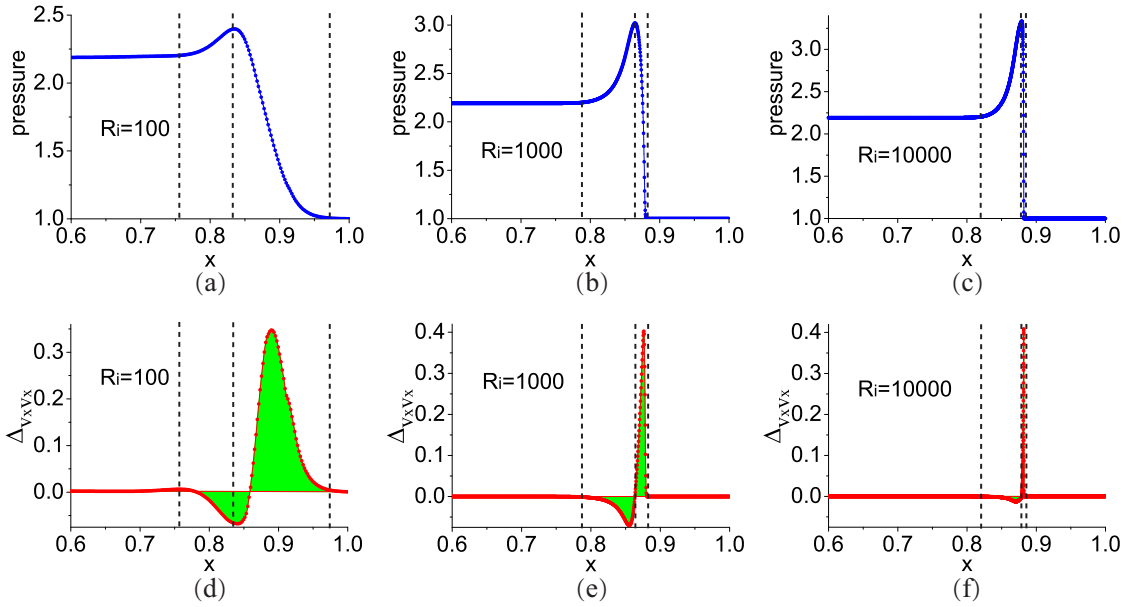


FIG. 11. (Color online) The physical quantities $p$ and $\Delta_{v_x v_x}$ versus $x$ at time $t = 0.35$. The first row is for the pressure and the second is for $\Delta_{v_x v_x}$. From left to right, the three columns are for $R_i = 10^2$, $R_i = 10^3$, and $R_i = 10^4$, respectively.

Consequently, $\Delta_{v_x v_x v_x}$, $\Delta_{v_x v_y v_y}$ deviate from zero in the reaction zone.

### B. Detonations from unsteady to steady: Simulations with different collision parameters

Now, we study detonation phenomena with different collision parameter sets: (i) $R_i = 10^2$, (ii) $R_i = 10^3$, (iii) $R_i = 10^4$. The first case here is just the case (i) in the above subsection. In the second case where $R_i = 10^3$, the parameters ($v_a$, $v_b$, $v_c$, $\eta_a$, $\eta_b$, $\eta_c$) = (2.7, 2.6, 1.9, 5.0, 0.0, 1.7), $\Delta x = 2 \times 10^{-4}$, $\Delta t = 2 \times 10^{-6}$, the other parameters are the same as the first case. In the third case where $R_i = 10^4$, the spatial and temporal steps $\Delta x = 4 \times 10^{-5}$, $\Delta t = 4 \times 10^{-6}$, the other parameters are the same as the second case.

Figure 11 shows the simulation results of $p$ and $\Delta_{v_x v_x}$ versus $x$ at time $t = 0.35$ in the three cases with $R_i = 10^2$, $R_i = 10^3$, and $R_i = 10^4$, respectively. Here we define ($X_m$, $P_m$) as the point where the largest pressure is located. The points in Figs. 11(a)–11(c) are (0.83450, 2.39850), (0.86410, 3.01965), and (0.87906, 3.33212), respectively. A vertical dashed guideline is plotted across this point in each panel. Aside from this guideline, another two lines are given to guide the eye for the width of the detonation wave. At the right side of the rightmost line is the unreacted explosive in thermodynamic equilibrium with zero reaction rate. At the left side of the leftmost line, where all the materials are reaction products, the system is in a constant state. From Figs. 11(a) to 11(c), the detonation wave at this time changes from unsteady to steady. It is interesting to study the TNE behaviors in these cases. The guidelines in Figs. 11(d)–11(f) coincide with those in Figs. 11(a)–11(c), respectively:

(1) It is clear to find in Figs. 11(a)–11(f) that the detonation wave, especially the preshocked area, becomes narrower with increasing $R_i$. Physically, the viscosity which is inversely proportional to $R_\mu$ widens the detonation wave, especially the preshocked area. Correspondingly, the area of nonequilibrium system is widened as well.

(2) Figures 11(a)–11(c) show that both $X_m$ and $P_m$ increase from left to right. That is to say, with the increase of $R_i$, it takes less time for the detonation to become steady, and the von Neumann peaks become higher and sharper. Physically, the viscosity expands and smooths the wavefront of pressure. Consequently, it decreases the local TNE effects.

(3) In Figs. 11(d)–11(f), the shaded area enclosed by the curve $\Delta_{v_x v_x}(x)$ and the line $\Delta_{v_x v_x} = 0$ decreases from left to right. This shaded area presents a rough description on the global TNE effect around the detonation wave in the system. From this sense, the viscosity increases the global TNE effect.

(4) The minimum of $\Delta_{v_x v_x}$ is $-0.06759$, $-0.07018$, $-0.01275$ in Figs. 11(d)–11(f), respectively. The corresponding maximum is 0.34753, 0.40275, 0.40857, respectively. The minimum of $\Delta_{v_x v_x}$ for $R = 1000$ is less than the other two, and the maximum for $R = 10\,000$ is the largest among the three cases. There is competition between the viscosity (heat conductivity) effect and the gradient effects of physical quantities ($\rho$, $\mathbf{u}$, $T$, $p$, etc.). With the increase of collision parameters, the viscosity and heat conductivity decrease, while the gradients of physical quantities increase. The former tend to decrease and the latter tend to increase the TNE effects. The physical reason is that the viscosity possesses both the thermodynamic and hydrodynamic functions. Thermodynamically, it tends to make the system approach the thermodynamic equilibrium more slowly. But hydrodynamically, it works as a kind of resistance force to the shocking process, makes the pressure curve smoother, and consequently tends to make the system deviate less from its thermodynamic equilibrium. The heat conductivity plays a similar role.

(5) The first horizontal position for $\Delta_{v_x v_x} = 0$ behind the von Neumann peak moves towards the horizontal position for the von Neumann peak as $R_i$ increases. It can be found a clear distance from the position for $\Delta_{v_x v_x} = 0$ to the position for the

von Neumann peak in Fig. 11(a), while the two points almost coincide in Fig. 11(c). That is to say, the position, where the internal energy in the $x$ degree of freedom equals to the average of all degrees of freedom, gets away from the position for the von Neumann peak with increasing viscosity.

## VII. CONCLUSION AND DISCUSSIONS

A MRT-LBKM for combustion phenomena is presented. The chemical energy released in the progress of combustion is dynamically coupled into the physical system by adding a chemical term to the LB kinetic equation. The chemical term describes the change rate of distribution function $f$ due to the local chemical reaction. Physically, the model is roughly equivalent with a Navier-Stokes model supplemented by a coarse-grained model of the thermodynamic nonequilibrium behaviors in the continuum limit. In this model the discrete equilibrium distribution function $f_i^{eq}$ needs to satisfy 24 independent kinetic moment relations. We present a discrete velocity model with 24 velocities which are divided into 3 groups. In each group, a flexible parameter ($v_a$, $v_b$, or $v_c$) is used to control the size of discrete velocities and a second parameter ($\eta_a$, $\eta_b$, or $\eta_c$) is used to describe the contribution of the extra degrees of freedom. The current model works for both subsonic and supersonic flows with or without chemical reaction. The rate equation for the chemical reaction can be adjusted according to specific situations. In the MRT-LBKM, the nonequilibrium behaviors of various modes may contribute to the system evolution according to different amplification factors.

As an initial application, various nonequilibrium behaviors around the detonation wave in one-dimensional detonation process are preliminarily probed. The following thermodynamic nonequilibrium behaviors, (i) exchange of internal kinetic energy between different degrees of freedom for molecule displacements, (ii) exchange of internal kinetic energy between the displacements and the extra degrees of freedom of the molecules, are observed. It is found that the system viscosity (or heat conductivity) decreases the local thermodynamic nonequilibrium, but increases the global thermodynamic nonequilibrium around the detonation wave, that even locally, the system viscosity (or heat conductivity) results in two kinds of competing trends, to increase and to decrease the thermodynamic nonequilibrium effects. The physical reason is that the viscosity (or heat conductivity) takes part in both the thermodynamic and hydrodynamic responses to corresponding driving forces. When we consider the thermodynamic nonequilibrium which can be described by various kinetic moments of $f - f^{eq}$, the Boltzmann equation (29) can be regarded as a kind of constitutive equation relating to the response $\hat{\mathbf{f}} - \hat{\mathbf{f}}^{eq}$, to the driving force $-\partial\hat{\mathbf{f}}/\partial t - \partial(\hat{\mathbf{E}}_\alpha\hat{\mathbf{f}})/\partial r_\alpha + \hat{\mathbf{A}} + \hat{\mathbf{C}}$. Thus, the inverse of the collision parameter $\hat{\mathbf{R}}^{-1}$ plays a role of the parameter describing material kinematic property. Thermodynamically, it tends to amplify the thermodynamic nonequilibrium effects. But hydrodynamically, the viscous force tends to decrease the pressure gradient, the heat conduction tends to decrease the temperature gradient, and consequently they tend to decrease thermodynamic nonequilibrium.

If the local temperature increment due to chemical reaction is dynamically taken into account in the calculation of local equilibrium distribution function $f_i^{eq}$ [78], the number of needed discrete velocities can be decreased to 16 in the two-dimensional case. In that case, only 12 nonconserved quantities are included in the two-dimensional MRT-LBKM.

## ACKNOWLEDGMENTS

The authors thank the anonymous referees and Professor S. Succi for helpful comments and suggestions on improving the manuscript, and thank Professor Z. Chen, Professor Y. Gan, and Professor H. Lai for fruitful discussions on modeling combustion and complex fluids. A.X. and G.Z. acknowledge support of the Science Foundations of National Key Laboratory of Computational Physics, National Natural Science Foundation of China (under Grants No. 11475028 and No. 11202003), the opening project of State Key Laboratory of Explosion Science and Technology (Beijing Institute of Technology) (under Grant No. KFJJ14-1M), and the Open Project Program of State Key Laboratory of Theoretical Physics, Institute of Theoretical Physics, Chinese Academy of Sciences, China (under Grant No. Y4KF151CJ1). Y.L. and C.L. acknowledge support of National Natural Science Foundation of China (under Grants No. 11074300 and No. 41472130), National Basic Research Program of China (under Grant No. 2013CBA01504).

[1] Y. Ju, Adv. Mech. **44**, 201402 (2014).
[2] S. Chu and A. Majumdar, Nature (London) **488**, 294 (2012).
[3] W. Jangsawang, B. Fungtammasan, and S. Kerdsuwan, Energy Convers. Manage. **46**, 3137 (2005).
[4] G. L. Schott, Phys. Fluids **8**, 850 (1965).
[5] F. A. Bykovskii, S. A. Zhdan, and E. F. Vedernikov, J. Propul. Power **22**, 1204 (2006).
[6] Y. Ju and K. Maruta, Prog. Energy Combust. Sci. **37**, 669 (2011).
[7] A. C. Fernandez-Pello, Proc. Combust. Inst. **29**, 883 (2002).
[8] J. L. Sabourin, D. M. Dabbs, R. A. Yetter, F. L. Dryer, and I. A. Aksay, ACS Nano **3**, 3945 (2009).
[9] Y. Ohkura, P. M. Rao, and X. Zheng, Combust. Flame **158**, 2544 (2011).
[10] J. E. Dec, Proc. Combust. Inst. **32**, 2727 (2009).
[11] A. Starikovskiy and N. Aleksandrov, Prog. Energy Combust. Sci. **39**, 61 (2013).
[12] M. Uddi, N. Jiang, E. Mintusov, I. V. Adamovich, and W. R. Lempert, Proc. Combust. Inst. **32**, 929 (2009).
[13] W. Sun, Z. Chen, X. Gou, and Y. Ju, Combust. Flame **157**, 1298 (2010).
[14] S. H. Won, B. Windom, B. Jiang, and Y. Ju, Combust. Flame **161**, 475 (2014).
[15] T. Ombrello, X. Qin, Y. Ju, A. Gutsol, A. Fridman, and C. Carter, AIAA J. **44**, 142 (2006).
[16] W. Sun, M. Uddi, S. H. Won, T. Ombrello, C. Carter, and Y. Ju, Combust. Flame **159**, 221 (2012).
[17] W. Sun and Y. Ju, J. Plasma Fusion Res. **89**, 208 (2013).
[18] D. L. Chapman, Philos. Mag. **47**, 90 (1899).

[19] E. Jouguet, J. Math. Pure Appl. **1**, 347 (1905).
[20] Ya. B. Zeldovich, J. Exp. Theor. Phys. **10**, 542 (1940) [Zhurnal Experimentalnoi i.Teoreticheskoi Fiziki. **10**, 542 (1940)].
[21] J. Von Neumann, *Theory of Detonation Waves* (Macmillan, New York, 1942).
[22] W. Doering, Ann. Phys. (NY) **435**, 421 (1943).
[23] W. Fickett and W. C. Davis, *Detonation: Theory and Experiment* (Dover, New York, 2000).
[24] Z. Chen, *Studies on the Initiation, Propagation, and Extinction of Premixed Flames* (Princeton University Press, Princeton, NJ, 2009).
[25] P. Dai, Z. Chen, S. Chen, and Y. Ju, Proc. Combust. Inst. **35**, 3045 (2015).
[26] H. Yu, W. Han, J. Santner, X. Gou, C. H. Sohn, Y. Ju, and Z. Chen, Combust. Flame **161**, 2815 (2014).
[27] B. Bai, Z. Chen, H. Zhang, and S. Chen, Combust. Flame **160**, 2810 (2013).
[28] Z. Y. Ren, Z. Lu, L. Y. Hou, and L. Y. Lu, Sci. China-Phys. Mech. Astron. **57**, 1495 (2014).
[29] C. J. Chen, R. A. Bernatz, K. D. Carlson, and W. Lin, *Finite Analyitic Method in Flow and Heat Transfer* (Taylor & Francis, London, 2000).
[30] F. J. Higuera, S. Succi, and R. Benzi, Europhys. Lett. **9**, 345 (1989).
[31] F. J. Higuera and J. Jimenez, Europhys. Lett. **9**, 663 (1989).
[32] R. Benzi, S. Succi, and M. Vergassola, Phys. Rep. **222**, 145 (1992).
[33] S. Succi, *The Lattice Boltzmann Equation for Fluid Dynamics and Beyond* (Oxford University Press, New York, 2001).
[34] S. Succi, I. V. Karlin, and H. Chen, Rev. Mod. Phys. **74**, 1203 (2002).
[35] H. Chen, S. Kandasamy, S. Orszag, R. Shock, S. Succi, and V. Yakhot, Science **301**, 633 (2003).
[36] G. Gonnella, E. Orlandini, and J. M. Yeomans, Phys. Rev. Lett. **78**, 1695 (1997).
[37] C. Denniston and J. M. Yeomans, Phys. Rev. Lett. **87**, 275505 (2001).
[38] G. Tóth, C. Denniston, and J. M. Yeomans, Phys. Rev. Lett. **88**, 105504 (2002).
[39] X. W. Shan and H. D. Chen, Phys. Rev. E **47**, 1815 (1993); **49**, 2941 (1994).
[40] S. Chen and G. D. Doolen, Annu. Rev. Fluid Mech. **30**, 329 (1998).
[41] Q. Kang, D. Zhang, S. Chen, and X. He, Phys. Rev. E **65**, 036318 (2002).
[42] H. Fang, Z. Wang, Z. Lin, and M. Liu, Phys. Rev. E **65**, 051925 (2002).
[43] Z. Guo and C. Shu, *Lattice Boltzmann Method and Its Applications in Engineering (Advances in Computational Fluid Dynamics)* (World Scientific, Singapore, 2013).
[44] A.-G. Xu, G.-C. Zhang, Y.-J. Li, and H. Li, Prog. Phys. **34**, 136 (2014), http://pip.nju.edu.cn/Home/ShowArticle/773.
[45] S. P. Dawson, S. Chen, and G. D. Doolen, J. Chem. Phys. **98**, 1514 (1993).
[46] J. R. Weimar and J. P. Boon, Phys. A (Amsterdam) **224**, 207 (1996).
[47] R. L. Zhang, Y. S. Xu, B. H. Wen, N. Sheng, and H. P. Fang, Sci. Rep. **4**, 5738 (2014).
[48] S. Chen, D. Martinez, and R. Mei, Phys. Fluids **8**, 2527 (1996).
[49] H. Lai and C. Ma, J. Stat. Mech. (2010) P04011; Phys. Rev. E **84**, 046708 (2011).
[50] S. Succi, G. Bella, and F. Papetti, J. Sci. Comput. **12**, 395 (1997).
[51] O. Filippova and D. Hänel, Int. J. Mod. Phys. C **9**, 1439 (1998).
[52] O. Filippova and D. Hänel, J. Comput. Phys **158**, 139 (2000).
[53] O. Filippova and D. Hänel, Comput. Phys. Commun. **129**, 267 (2000).
[54] H. Yu, L. S. Luo, and S. S. Girimaji, Int. J. Comput. Eng. Sci. **3**, 73 (2002).
[55] K. Yamamoto, X. He, and G. D. Doolen, J. Stat. Phys. **107**, 367 (2002).
[56] K. Yamamoto, Int. J. Mod. Phys. B **17**, 197 (2003).
[57] K. Yamamoto, N. Takada, and M. Misawa, Proc. Combust. Inst. **30**, 1509 (2005).
[58] T. Lee, C. Lin, and L. D. Chen, J. Comput. Phys. **215**, 133 (2006).
[59] E. Chiavazzo, I. V. Karlin, A. N. Gorban, and K. Boulouchos, Combust. Flame **157**, 1833 (2010).
[60] S. Chen, Z. Liu, C. Zhang, Z. He, Z. Tian, B. Shi, and C. Zheng, Appl. Math. Comput. **193**, 266 (2007).
[61] S. Chen, Z. Liu, Z. Tian, B. Shi, and C. Zheng, Comput. Math. Appl. **55**, 1424 (2008).
[62] S. Chen and M. Krafczyk, Int. J. Therm. Sci. **48**, 1978 (2009).
[63] S. Chen, Int. J. Hydrogen Energy **35**, 1401 (2010).
[64] S. Chen, J. Li, H. Han, Z. Liu, and C. Zheng, Int. J. Hydrogen Energy **35**, 3891 (2010).
[65] S. Chen, H. Han, Z. Liu, J. Li, and C. Zheng, Int. J. Hydrogen Energy **35**, 4736 (2010).
[66] S. Chen and C. Zheng, Int. J. Hydrogen Energy **36**, 15403 (2011).
[67] S. Chen, J. Mi, H. Liu, and C. Zheng, Int. J. Hydrogen Energy **37**, 5234 (2012).
[68] A. Xu, G. Zhang, Y. Gan, F. Chen, and X. Yu, Front. Phys. **7**, 582 (2012).
[69] F. J. Alexander, H. Chen, S. Chen, and G. D. Doolen, Phys. Rev. A **46**, 1967 (1992).
[70] F. J. Alexander, S. Chen, and J. D. Sterling, Phys. Rev. E **47**, R2249 (1993).
[71] Y. Chen, H. Ohashi, and M. Akiyama, Phys. Rev. E **50**, 2776 (1994).
[72] G. R. McNamara, A. L. Garcia, and B. J. Alder, J. Stat. Phys. **87**, 1111 (1997).
[73] M. Watari and M. Tsutahara, Phys. Rev. E **67**, 036306 (2003).
[74] F. Chen, A. Xu, G. Zhang, Y. Li, and S. Succi, Europhys. Lett. **90**, 54003 (2010).
[75] F. Chen, A. Xu, G. Zhang, and Y. Wang, Front. Phys. **9**, 246 (2014).
[76] Y. Gan, A. Xu, G. Zhang, and Y. Yang, Europhys. Lett. **103**, 24003 (2013).
[77] C. Lin, A. Xu, G. Zhang, Y. Li, and S. Succi, Phys. Rev. E **89**, 013307 (2014).
[78] B. Yan, A. Xu, G. Zhang, Y. Ying, and H. Li, Front. Phys. **8**, 94 (2013).
[79] C. Lin, A. Xu, G. Zhang, and Y. Li, Commun. Theor. Phys. **62**, 737 (2014).
[80] P. Lallemand and L. S. Luo, Phys. Rev. E **61**, 6546 (2000); **68**, 036706 (2003).
[81] H. Zhang and F. Zhuang, Adv. Appl. Mech. **29**, 193 (1991).
[82] S. G. Cochran and J. Chan, Shock Initiation and Detonation in One and Two Dimensions, Lawrence Livermore National Laboratory Report No. UCID-18024, 1979 (unpublished).